Chapter 3
Cyclodextrins and Nanostructured Porous Inorganic Materials

Rudina Bleta, Eric Monflier, and Anne Ponchel

Contents

Abstract The discovery of ordered mesoporous materials in 1992 by Mobil Oil Corporation (Mobils) scientists has opened great opportunities for new applications in many emerging fields such as heterogeneous catalysis, biocatalysis, energy conversion, biosensors, photocatalytic devices and environmental technologies. Porous materials are grouped by the International Union of Pure and Applied Chemistry (IUPAC) into three classes according to their pore diameter: microporous (< 2 nm), mesoporous (2–50 nm) and macroporous (> 50 nm). One of the most versatile methods for the preparation of these materials is the soft-template approach which combines the sol-gel process with the molecular self-assembly. Materials with monodisperse particle sizes, well-defined architectures and tunable porosity can be built by this approach using micelles formed by ionic or non-ionic surfactants, as well as amphiphilic polymers, as templates. On the other hand, the supramolecular

R. Bleta (✉) · E. Monflier · A. Ponchel
Univ. Artois, CNRS, Centrale Lille, ENSCL, Univ. Lille, UMR 8181,
Unité de Catalyse et Chimie du Solide (UCCS), F-62300 Lens, France
e-mail: rudina.bleta@univ-artois.fr

S. Fourmentin et al. (eds.), *Cyclodextrin Fundamentals, Reactivity and Analysis*,
Environmental Chemistry for a Sustainable World,
https://doi.org/10.1007/978-3-319-76159-6_3

assemblies formed between cyclodextrins and block copolymers have been less investigated in the literature for the preparation of inorganic materials or nanocomposites, despite their large chemical and structural diversity.

This chapter focuses mainly on nanostructured porous inorganic materials derived from cyclodextrins or cyclodextrin-based assemblies. Examples from literature (more than 100 references) are described and discussed, in which we look both at the synthesis and characterization of those materials, as well as their applications in photocatalysis and heterogeneous catalysis. We first give a brief introduction to mesoporous silica prepared from conventional surfactants and polymers, and then look at attempts to the development of new synthetic strategies using cyclodextrin-based assemblies specifically designed to meet specific applications. Thus, cyclodextrin-based poly*pseudo*rotaxanes have been successfully used as templates for the preparation of mesoporous SiO_2 with tunable porosity. Moreover, multiple levels of porosity have been also integrated within the same structure, yielding silica materials with accessible porosities and hierarchical order at multiple length scales. On the other hand, for transition metal oxides, which are more difficult to prepare *via* the direct templating approach due to the very fast hydrolysis and condensation of the corresponding alkoxides in aqueous phase, the template-directed colloidal self-assembly approach is preferred and described. This approach involves the use of pre-synthesized colloidal particles which have the ability to self-assemble around a soft template (e.g., block copolymer or biopolymer). After drying and calcination, the recovered materials are usually robust and present high surface areas, large pore volumes and tunable porosities. For instance, supramolecular assemblies prepared from the randomly methylated β-cyclodextrin (RaMeβ-CD) have been successfully used as soft templates for the preparation of metal oxide nanostructures, such as TiO_2 and Al_2O with tunable properties.

From the perspective of applications, this book chapter presents recent developments involving the use of this new class of cyclodextrin-derived porous materials and nanocomposites in the emerging fields of heterogeneous catalysis and photocatalysis. A special attention is paid to the evaluation of the critical parameters that need to be controlled for improving their (photo) catalytic performances.

3.1 Introduction

Nanostructured porous materials have attracted tremendous research interest during the past two decades due to their unique structural and functional properties (Davis 2002; Lu and Schüth 2006; Imhof and Pine 1997; Velev and Kaler 2000). As reported in a large number of well-documented reviews, these materials offer potential applications in many emerging fields such as heterogeneous catalysis, energy conversion and storage devices, electrochemistry, optics, membranes and separation, drug delivery, biocatalysis, biosensors, photocatalytic devices and environmental technologies (Corma 1997;Sun et al. 2016; Zhu et al. 2015; Walcarius 2013).

Although a wide range of synthesis and assembly strategies have been developed so far for the fabrication of materials with tunable properties, the template synthesis remains one of the most flexible and important approaches to generate self-assembled nanostructures with well-defined architectures and hierarchical order at multiple length scales (Velev and Kaler 2000; Bleta et al. 2006; Blin et al. 2006; Liu et al. 2013; Yang et al. 2017). As both the structure and the composition of the template play a crucial role in the properties of the resulting material, there is a need to develop new supramolecular templates with tailored properties. In this context, cyclodextrins are of special interest owing to their unusual structural polymorphism as well as their ability to generate, in association with polymers, a wide range of fascinating supramolecular architectures (Wenz 1994; Born and Ritter 1995; Harada 1996; Herrmann et al. 1997; Szejtli 1998; Breslow and Dong 1998; Harada 2001).

In this book chapter, we aim to highlight the recent developments on the use of the native and modified cyclodextrins, as well as the supramolecular assemblies that they form by host-guest interactions with polymers, as excellent candidates for fabricating inorganic materials with precise control over the pore size and structure, the particle shape, the crystal phase composition and the spatial arrangement of nanoparticles. The three main topics that we aim to highlight are: (1) the use of nanocasting as a flexible and versatile strategy for replicating the architecture of cyclodextrin-based aggregates, poly*pseudo*rotaxanes and three-dimensional hydrogels to create hierarchically structured porous silica materials with well-defined spatial arrangement of the mico-, meso- and macropores, (2) elaboration of nanostructured metal oxide materials, other than silica, by template-directed colloidal self-assembly using cyclodextrin-based supramolecular assemblies as soft template and sol-gel synthesized colloidal particles as building blocks; (3) some applications of these materials in the emerging fields of heterogeneous catalysis and photocatalytic degradation of pesticides from wastewater.

3.2 Natural Porous Materials and Biomimetic Design

Porous materials occur widely in nature. Diatoms and radiolarians are most famous examples of natural porous materials living in most aquatic environments and using photosynthesis as a source of energy. One of the most remarkable features of these unicellular microalgae is their cell wall which is build-up of a silicified shell, also known as frustule. The diatom frustule displays a highly porous hierarchical structure and exhibits an extremely high mechanical stability which can be retained over geological timescales (Kooistra et al. 2007). Moreover, diatoms also play a major role in the carbon cycle of our Earth since they produce through photosynthesis about one-fifth of the oxygen we breathe (Kröger and Poulsen 2008). They act therefore as major contributors to global carbon dioxide fixation (Armbrust 2009).

Diatoms can be recognized in a microscope by their highly ornamented frustule (Fig. 3.1) (Hildebrand 2008). The diatom frustule is partly organic (proteins and

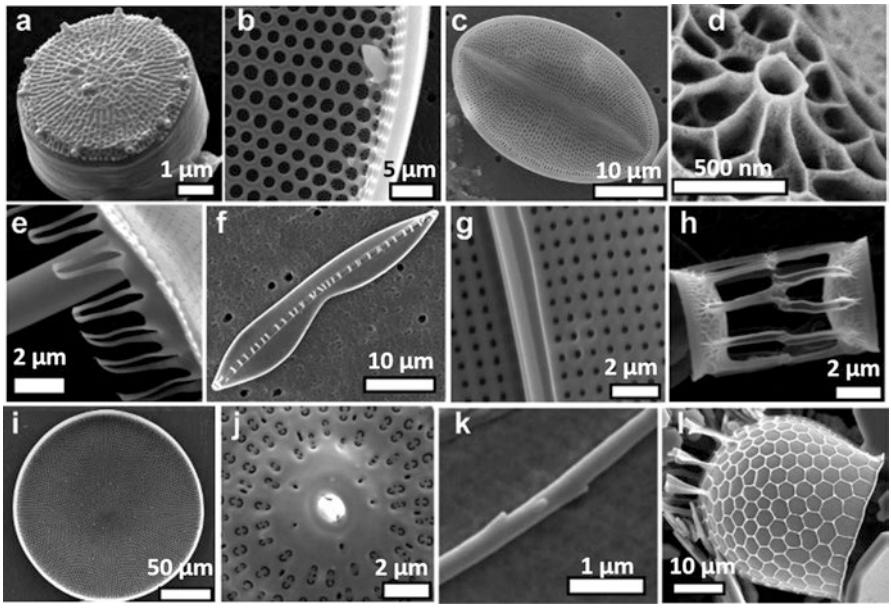

Fig. 3.1 Diversity of diatom silica structures. Acid-cleaned material from (**a**) *Thalassiosira pseudonana,* (**b**) close up of *Coscinodiscus wailesii*, (**c**) *Cocconeis sp.*, (**d**) rimoportula from *Thalassiosira weissflogii*, (**e**) corona structure *of Ditylum brightwellii*, (**f**) *Bacilaria paxillifer*, (**g**) close up of pores in *Gyrosigma balticum*, (**h**) *Skeletonema costatum*, (**i**) valve of *C. wailesii*, (**j**) close up of pores in *D. brightwellii*, (**k**) seta of *Chaetoceros gracilis*, and (**l**) *Stephanopyxis turris*. Reprinted with permission from (Hildebrand 2008). Copyright 2008 American Chemical Society

polysaccharides) and partly bioinorganic (hydrated silicon, $SiO_2{\cdot}[H_2O]_n$) and is formed through a remarkably rapid biomineralization process that is accomplished under mild physiological condition (Sumper et al. 2007). The frustule presents a well-defined hierarchical structure where several nanoscale elements (pores, channels) are regularly arranged in a complex 3D architecture with high level of precision. This porous structure is incredibly robust and confers to diatoms remarkable properties, such as mechanical strength, density, permeability, color and hydrophobicity, which protect them against desiccation, grazers and parasites (Hamm et al. 2003).

Pioneering biochemical studies of frustule composition have been performed by Kröger *et al.* in the diatom *Cylindrotheca fusiformis* and have led to the identification of three groups of biopolymers, *i.e.* the silaffins, the silacidines and the long chain polyamines, acting as major contributors in the biosilification process (Kröger and Poulsen 2008; Kröger et al. 1999). Silaffins and silacidins are peptides or proteins that carry many phosphate residues attached to amino acids (serine and threonine), whereas long chain polyamines are essentially linear non-protein components consisting of oligo-propyleneimine chains. Through self-assembly processes, essentially under electrostatic control, these biomolecules form bio-aggregates. Both the size of the aggregates and the quantity of the silicic oligomers that bind

them determine the final size of the silica spheres in the architecture of the diatom frustule.

The recent sequencing of the genome in diatom *Thalassiosira pseudonana* greatly simplified the identification of silaffin genes and qualified these species as model organisms in future research on silica biomineralization (Armbrust et al. 2004; Poulsen and Kröger 2004). It was found that some rules exist during the construction of the diatom frustule implicating the action of an enzymatic machinery which transforms the amino acid sequence information within the silaffin polypeptide into the observed modified pattern. The structure of these silaffin polypeptides was found to influence the self-assembly process which guides the silica formation. Understanding the mechanism of fabrication of the diatom frustule is an inspiration for developing new synthetic routes towards novel structures that mimic natural systems.

3.3 Main Strategies toward the Synthesis of Nanostructured Silica Materials

3.3.1 The Concept of Nanocasting

Over the past 25 years, since the discovery of mesoporous materials by the group of Mobil Oil Corporation (Kresge et al. 1992; Beck et al. 1992), many research groups have proposed different biomimetic approaches to build nanostructured materials with multi-scale porous structures, similar to those of diatoms. One of the most well-known approaches is the nanocasting route. This approach has proved to be straightforward and highly effective for the synthesis of nanosystems that are able to mimic the original structure of a template (Wan and Zhao 2007). Generally, two kinds of templates, defined as hard- and soft-templates, are described in the literature. Hard templates are solid-state materials with particular structure and morphology, such as mesoporous silica, usually used for the synthesis of ordered carbon materials. On the other hand, soft templates are usually in a fluid-like state and have attracted more attention for the synthesis of mesoporous solids with tailorable pore structures.

Various supramolecular assemblies prepared from ionic or non-ionic surfactants or water-soluble polymers can be used as soft templates to prepare well-ordered mesoporous silica with monodisperse pore sizes (Lu and Schüth 2006). Most common mesoporous silicas are the small pore hexagonal Mobil Composition of Matter-41 (MCM-41), cubic MCM-48, lamellar MCM-50, the large pore hexagonal Santa Barbara Amorphous-15 (SBA-15) and cubic SBA-16, as well as Hexagonal Mesoporous Silica (HMS) and Michigan State University (MSU) materials with wormlike pore structure (Fig. 3.2).

Most of them are prepared quite easily, under mild conditions, using the sol-gel process. The sol-gel synthesis involves the hydrolysis and catalytic polycondensation

Fig. 3.2 Different types of mesoporous materials. (**a**) Hexagonal arrangement of pores: type Mobil Composition of Matter-41 (MCM-41); (**b**) Cubic arrangement of pores: type MCM-48; (**c**) Lamellar arrangement of pores: type MCM-50. Reprinted with permission of the Royal Society of Chemistry from (Corma et al. 2008)

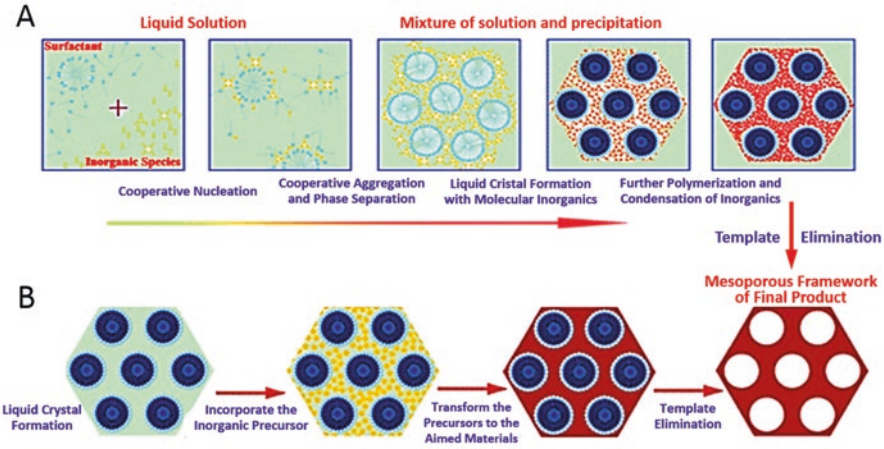

Fig. 3.3 Schematic representation of the soft-templating method *via* two synthetic strategies: (**A**) cooperative self-assembly and (**B**) "true liquid-crystal templating" (TLCT) process for the synthesis of ordered mesoporous materials. Reprinted with permission from (Wan and Zhao 2007). Copyright 2007 American Chemical Society

of a silicon alkoxide precursor (e.g., tetramethoxysilane or tetraethoxysilane) in the presence of a supramolecular template (typically micelles formed by amphiphilic molecules). The macromolecular network of siloxane bonds can be obtained by two different ways, *i.e. via* a cooperative assembly process taking place in-situ between the structure directing agent and the silica precursor in solution, or through a true liquid-crystal-phase templating (TLCT) mechanism, by formation of a silica framework around the pre-formed liquid crystal mesophase (Fig. 3.3). It is worth emphasizing that the cooperative assembly process is not a nanocasting route since it does not replicate a preformed surfactant structure. For instance, in the synthesis of mesoporous silica, concentrations of surfactant even below the critical micelle concentration (CMC) can yield highly ordered mesoporous structures. These materials are usually highly porous (pore volume higher than 0.7 $cm^3\ g^{-1}$), possess

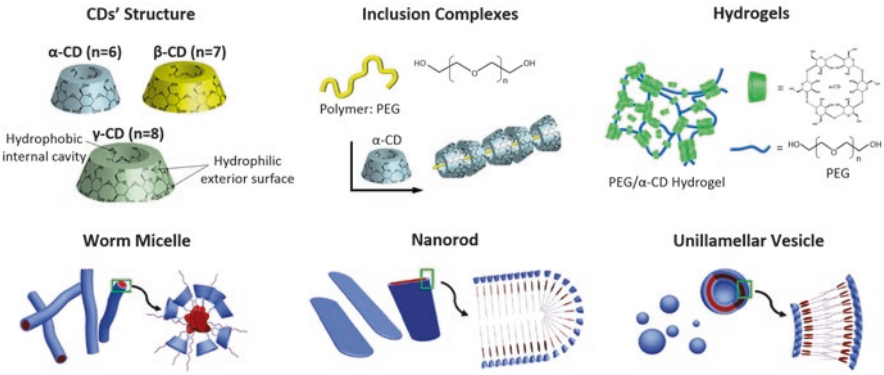

Fig. 3.4 Cyclodextrins structure and cyclodextrin-based nanosystems formed by their self-assembly with polymers. Adapted with permission from (Harada et al. 2009) and (Jiang et al. 2010). Copyright 2009 and 2010 American Chemical Society

large specific surface areas (up to 1500 $m^2\ g^{-1}$), well-defined multiscale porous networks, tunable pore sizes and interconnectivity. These properties make them viable for applications in different emerging fields ranging from biotechnology, biomedicine, drug delivery, catalysis, energy storage, optics, separation processes to immobilization of biomolecules and bio-organisms as well as bone regeneration (Su et al. 2012).

3.3.2 Using Cyclodextrin-Based Supramolecular Assemblies as Templates

The structure and properties of the template play a crucial role with respect to the properties of the replicated porous materials. In this context, cyclodextrins (CDs) offer attractive alternative to surfactants owing to the rich structural diversity of the supramolecular assemblies that they form in aqueous phase in association with polymers. Cyclodextrins are water-soluble cyclic oligosaccharides composed of a hydrophobic internal cavity and a hydrophilic exterior surface due to the presence of a large number of hydroxyl groups. Most common cyclodextrins contain six (α-CD), seven (β-CD) or eight (γ-CD) glucopyranose units in the ring (Fig. 3.4). These molecules demonstrate multifunctional properties, such as the ability to form supramolecular assemblies with a large variety of intriguing structures with amphiphilic surfactants of appropriate size and shape (Szejtli 1998; Breslow and Dong 1998; Wenz 1994; Born and Ritter 1995; Harada 2001; Harada 1996; Herrmann et al. 1997) (Fig. 3.4). Since the pioneering works of Harada *et al.* (Harada and Kamachi 1990), who showed that α-CD can form inclusion complexes with poly(ethylene glycol) (PEG) in aqueous solution to give poly*pseudo*rotaxanes with a necklace-like structure, a range of polymeric guests have been investigated

(Harada et al. 2009). A particular attention has been paid to the interactions occurring between the native β-CD and nonionic triblock copolymers of the poly(ethylene oxide) (PEO)-*b*-poly(propylene oxide) (PPO)-*b*-poly(ethylene oxide) (PEO) family, also known as Pluronics. Thus, it has been shown that the native β-CD can slide along the hydrophilic extremity PEO blocks of the Pluronic P84 ($PEO_{19}PPO_{43}PEO_{19}$) to selectively thread the middle hydrophobic PPO blocks and form poly*pseudo*rotaxanes with a well-ordered channel structure.

Despite their rich structural polymorphism, the supramolecular assemblies formed between block copolymers and CD-derivatives have been very little used as soft templates. In the field of materials science, micelles and lyotropic phases are the most commonly used templates for the synthesis of porous materials with controlled architectures. On the other hand, the possibility of using CDs or CD/polymer assemblies as supramolecular templates have been reported only in few studies and most of them have been devoted to the synthesis of mesoporous silica by sol-gel process (Polarz et al. 2001; Han and Antonietti 2002; Han et al. 2003).

3.3.3 Microporous Silica from Cyclodextrins

The possibility to extend the principle of nanocasting from micelles and lyotropic phases to cyclodextrins was first demonstrated by Antonietti *et al.* (Polarz et al. 2001; Polarz and Antonietti 2002; Antonietti 2006) who employed the aggregates formed by native and modified cyclodextrins in water as templates in the nanocasting process. Cyclodextrins have the ability to self-assemble in water into assemblies with a "molecular barrel" structure (Saenger 1980). These "barrels" have an exterior surface covered by -OH groups, while the interior cavity is quite hydrophobic, characterized by exposure of $-CH_2-$ groups. Owing to the rich OH-functionality on their outside surface, cyclodextrin assemblies in water can be nanocasted. Interestingly, the silica materials prepared by nanocasting were "worm-type" and presented a very similar structure to those obtained with classical amphiphiles (Fig. 3.5). The pore morphology did not agreed with the structure of a molecularly dispersed system, thus confirming the formation of cyclodextrin aggregates that can be replicated by nanocasting. The pore size corresponded exactly to the diameter of the cyclodextrin, while the length was significantly larger. The pore cross-section of these materials, as determined by porosimetry, was directly related to the diameter of the single circular dichroism (CD)-units. Thus, using the hydroxypropylated α-CD (HPα-CD) assemblies, 1.4 nm pores were obtained, while the replication of the HPγ-CD assemblies led to 1.8 nm pores. Such a direct correlation is an important indication that the pore systems results really from the "molecular barrel" structure of the CD assemblies. The difference between the hydrophilic exterior and the hydrophobic interior of the CD-molecule was supposed to be the driving force for this assembly.

This result was particularly interesting since it showed for the first time that, besides offering the possibility to synthesize nanostructured silica materials,

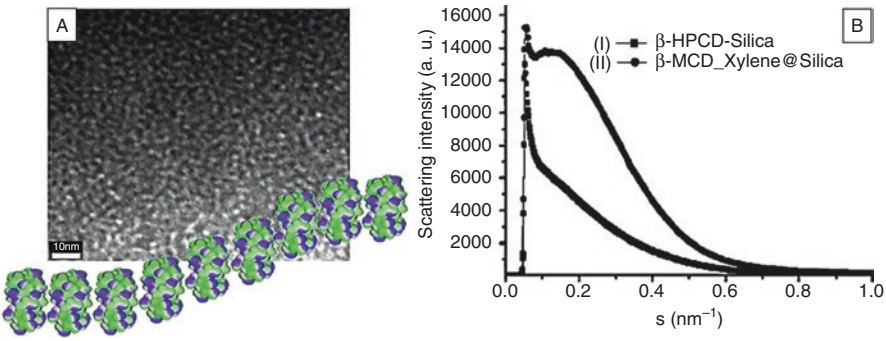

Fig. 3.5 (**A**) Transmission electron microscopy (TEM) image of a representative CD-based silica demonstrating the 'worm-type' architecture of the pores and a schematic image of the CD-alignment indicating the template structure; (**B**) small angle X-ray scattering (SAXS) diffractograms of two CD-based porous materials: (i) one was prepared using the hydrophilic β-HPCD showing a rather disordered pore-system, (ii) the other one was prepared with xylene@β-MCD possessing strong quadrupolar amphiphilic character. The latter pore-system is much more ordered and uniform. Reprinted with permission of the Royal Society of Chemistry from (Polarz and Antonietti 2002)

nanocasting can also be used as "analytical tool" to examine the soft and delicate structure of these assemblies. Thus, instead of investigating the soft-matter structure in its dispersion medium itself, it is possible to examine its "hardcopy" derived by nanocasting. This route has several potential advantages in comparison with the direct examination due to the higher electron contrast and higher stability of the solid matter against most experimental conditions, such as electron microscopy or scattering techniques.

3.3.4 *Mesoporous Silica from Cyclodextrin-Based poly*pseudo*rotaxanes*

Besides cyclodextrins, poly*pseudo*rotaxanes can also be replicated into mesoporous silica (Han and Antonietti 2002). It has been reported that in the case of triblock copolymers, the native α-CD preferentially binds the PEO units, whereas the native β-CD can slide along the hydrophilic extremity PEO blocks to selectively thread the middle hydrophobic PPO blocks (Harada 1996; Harada et al. 2009). The resulting poly*pseudo*rotaxanes have "string-of-pearl" morphologies. The structural models proposed by Harada (Harada 1996) for these channel-like inclusion complexes are depicted in Fig. 3.6. Remarkably, these poly*pseudo*rotaxanes were shown to spontaneously self-assemble in water to generate other types of supramolecular assemblies with a well-defined crystalline structure. Thus, by using small-angle neutron scattering (SANS) and atomic force microscopy (AFM), it was demonstrated that the self-assembly of β-CD and Pluronic F68 ($PEO_{80}PPO_{27}PEO_{80}$) micelles may lead to the formation of cylindrical bundles, which can then act as building blocks

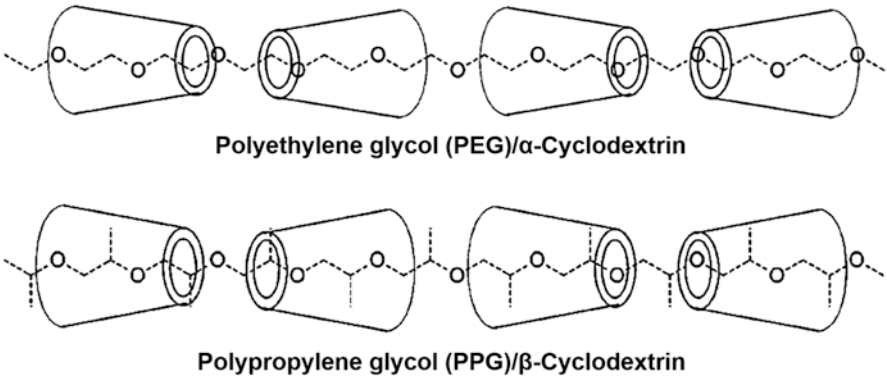

Fig. 3.6 Poly*pseudo*rotaxanes formed by threading of α-cyclodextrin along polyethylene glycol and β-cyclodextrin along polypropylene glycol. Reprinted with permission from (Han and Antonietti 2002). Copyright 2002 American Chemical Society

for the formation of flat and rigid platelets with well-defined angles at 40 °C (Travelet et al. 2008; 2009; 2010). When these *in-situ* formed supramolecular assemblies were used as templates for the synthesis of silica materials, the pore diameter was found to depend on the pH of the solution (Han and Antonietti 2002). Direct replication was obtained at pH 2.0, whereas larger pores were formed at higher pH values between pH 3 and pH 4 (Fig. 3.7). Usually, the structure of the formed silica does not change strongly in the pH range between 2.0 and 4.0. Therefore, the increase in the pore size was directly related to a pH-dependent behavior of the template. Accordingly, poly*pseudo*rotaxanes aggregate at pH 4.0 into arrays or bundle structures that can generate larger pores by nanocasting.

The nanocasting procedure was also extended to stable isolated poly*pseudo*rotaxanes obtained from α-CD and polyamines (Han et al. 2003). The obtained silica materials possessed elongated mesopores and high porosity. An approximate replica of the original rod-like rotaxanes was produced with a homogeneous distribution of the pores in the silica matrix.

3.3.4.1 Hierarchically Porous Silica from Polyethylene Glycol/α--Cyclodextrin Hydrogels

Not only cyclodextrin barrels or poly*pseudo*rotaxanes, but also highly reticulated hydrogels and their self-assembly motifs, can be replicated. This was clearly illustrated by silicification by sol-gel process of the polyethylene glycol/α--cyclodextrin (PEG/α-CD) hydrogels that yielded nanostructured silica materials with bimodal or trimodal pore size distributions (Fig. 3.8) (Bleta et al. 2014c).

Hydrogels can be defined as water-swollen hydrophilic polymers, formed by covalent bonds or physical cohesion forces between the polymer segments, such as van der Waals forces, hydrophobic interactions or hydrogen bonds. The pioneering

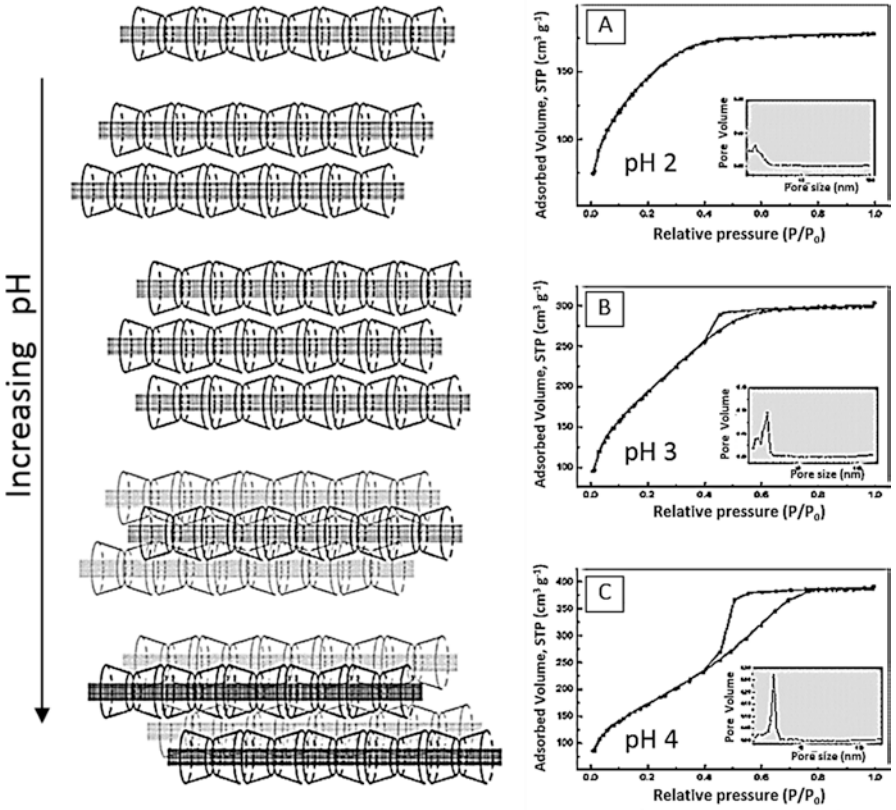

Fig. 3.7 Schematics of the pH-dependent aggregation of poly*pseudo*rotaxanes of polyethers with cyclodextrins. At pH 2.0, a single poly*pseudo*rotaxane domain predominates. With increasing pH values (pH 3.0 and 4.0), the aggregation of poly*pseudo*rotaxanes is enhanced giving bundle domains. N_2-sorption data of the three silicas prepared from α-cyclodextrin and polyethylene glycol (PEG) 2000 condensed at pH 2.0 (**A**), 3.0 (**B**) and 4.0 (**C**). Insets: pore size distribution as calculated by the Barrett-Joyner-Halenda (BJH) theory from the desorption branch. Reprinted with permission from (Han and Antonietti 2002). Copyright 2002 American Chemical Society

work of Li et al. (Li et al. 1994) showed that the native α-CD and a high molecular weight PEG (higher than 10,000 g mol^{-1}) can spontaneously form a three-dimensional physically cross-linked hydrogel by host-gust interactions. A large amount of water can be entrapped within the macroscopic voids. Gelation was proposed to occur *via* the cross-linking of the partially formed PEG/α-CD inclusion complex, which further self-assemble into water insoluble poly*pseudo*rotaxanes with a channel-like structure (Li et al. 1994). Subsequently, the individual poly*pseudo*rotaxanes further grow in size, aggregate and finally phase-separate. As stated by Weickenmeier and Wenz (Weickenmeier and Wenz 1997), the phase-separation is followed by the threading of additional α-CD onto the polymer chains, leading to the aggregation and growth of columnar poly*pseudo*rotaxane-based

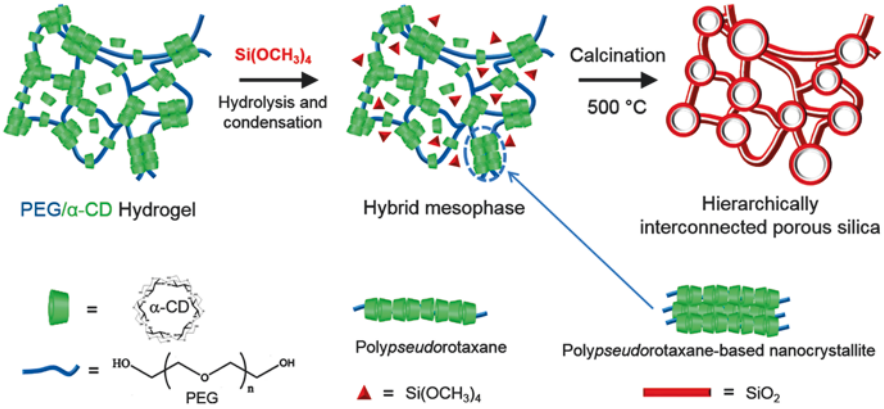

Fig. 3.8 Schematic illustration of the template-directed synthesis of silica materials with hierarchical pore architectures where the large mesopores are interconnected by small mesopores in a three-dimensional framework. The crosslinking of these poly*pseudo*rotaxanes into columnar nanocrystallites with a channel-like architecture directs the condensation of silica in a bi- or tri-modal porous network. Reprinted with permission of the Royal Society of Chemistry from (Bleta et al. 2014c)

nanocrystallites (Travelet et al. 2009, 2010). This nanoscale arrangement of poly*pseudo*rotaxanes into nanocrystallites is assumed to play a crucial role in maintaining the hydrogel in a water-swollen state.

To investigate in detail how the PEG concentration affects the gelation behavior, a series of silica materials were prepared by templating the hydrogels prepared with increasing amounts of PEG (1–30 mg mL^{-1}) in a saturated α-CD solution (100 mg mL^{-1}) at pH 4 and 2 (Bleta et al. 2014c). The chemistry of silica does not change significantly in this pH range, which is close to the isoelectric point of silicic acid, where the condensation rate is the slowest. So, the variations monitored in the porosity of the materials can be mainly attributed to the structural changes occurring within the hydrogel template in response to pH.

The adsorption isotherms and corresponding pore size distributions of the silica materials prepared at pH 4 are shown in Fig. 3.9A. In contrast to the materials prepared from PEG alone (average pore size 2.0 nm), those prepared from α-CD alone showed a well-defined type IV isotherm with a pronounced hysteresis loop typical of a mesoporous material. Mesopores have an average diameter of 6.8 nm which can be associated with the formation of large α-CD aggregates in water. Interestingly, when a small amount of PEG (1 mg mL^{-1}) was added to the saturated α-CD solution (100 mg mL^{-1}), two populations of small mesopores were observed at 1.8 nm and 2.0 nm attributed to the naked polymer chains and poly*pseudo*rotaxanes made from α-CD threaded onto PEG in a dynamic threading-dethreading equilibrium. For higher PEG concentrations (4–30 mg mL^{-1}), the examination of the pore structure of the resulting materials gave evidence of a hierarchical pore structure with three types of pores: (i) micropores (1.8 nm) associated with naked polymer chains, (ii) small mesopores (2.0 and 2.3 nm) associated with individual

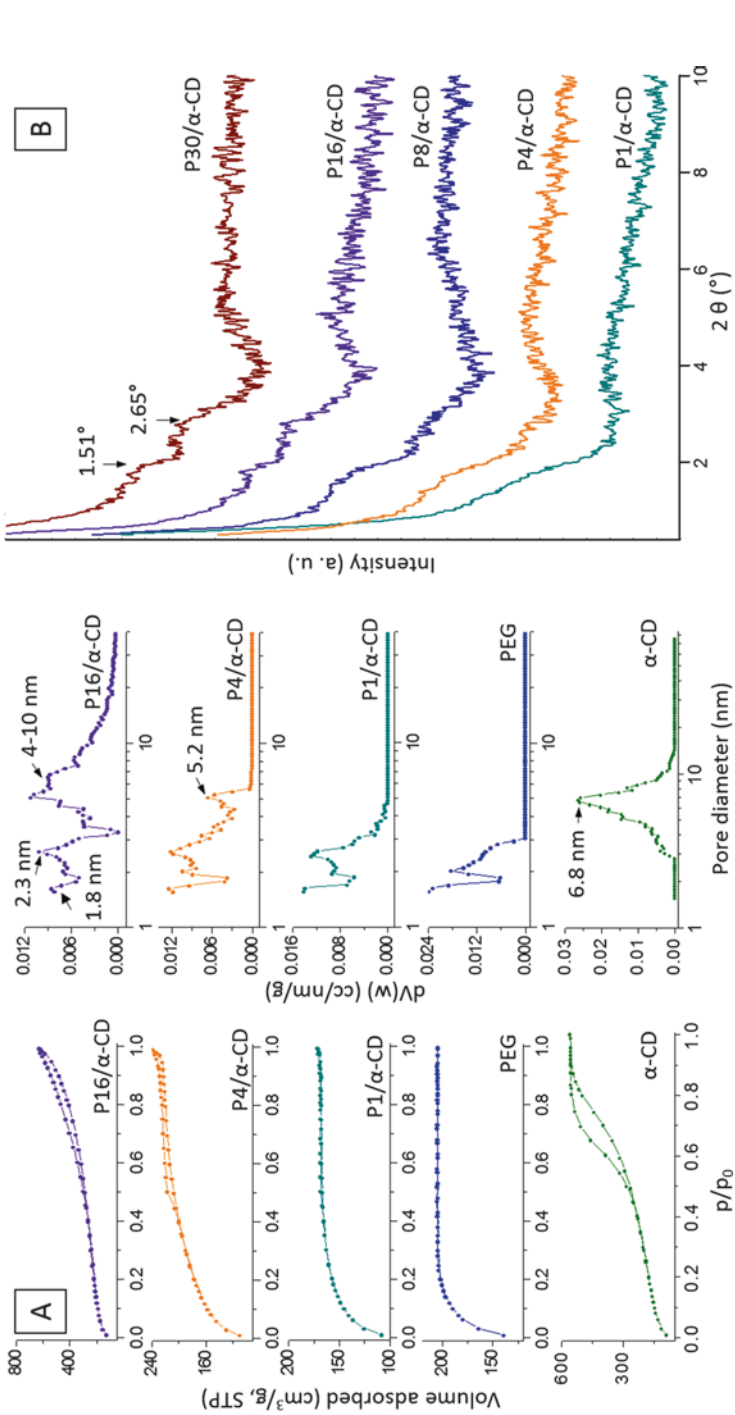

Fig. 3.9 (A) N_2-adsorption isotherms and corresponding pore size distributions determined by non-local density functional theory (NLDFT) for silica prepared at pH 4 from a saturated α-CD solution (100 mg mL^{-1}), from PEG (16 mg mL^{-1}) and from PEG/α-CD mixtures prepared with increasing amounts of polymer, from 1 mg mL^{-1} (P1) to 16 mg mL^{-1} (P16). With increasing PEG concentration, the aggregation of poly*pseudo*rotaxanes is enhanced giving rise to three types of pores: micropores (1.8 nm) associated with naked polymer chains, small mesopores (2.0 and 2.3 nm) associated with individual poly*pseudo*rotaxanes and larger mesopores (5.8 nm) associated with the columnar α-CD crystallites formed by the self-assembly of poly*pseudo*rotaxanes. (B) Corresponding small angle X-ray scattering (SAXS) plots. All samples were calcined at 500 °C for 16 h. Adapted with permission of the Royal Society of Chemistry from (Bleta et al. 2014c)

Table 3.1 Textural characteristics of the silicified α-CD after calcination at 500 °C

Sample	S_{BET} ($m^2\ g^{-1}$)	V_{cum} ($cm^3\ g^{-1}$)	PS (nm)	V_{micro} ($cm^3\ g^{-1}$)	% micro
CD100-pH 4	634	0.839	6.8	0.001	0.2
Bare PEG-pH 4	688	0.309	2.0	0.195	63
P1CD100-pH 4	639	0.251	2.0 and 2.3	0.140	56
P2CD100-pH 4	607	0.242	2.0 and 2.3 and 5.2	0.111	46
P4CD100-pH 4	618	0.338	2.0 and 2.3 and 5.2	0.086	26
P8CD100-pH 4	663	0.755	2.0 and 4–10	0.062	8.2
P16CD100-pH 4	777	0.912	2.0 and 4–10	0.075	8.2
P30CD100-pH 4	760	0.979	2.0 and 4–10	0.026	2.7
Bare PEG-pH 2	545	0.249	2.0	0.184	74
P4CD100-pH 2	635	0.373	2.0 and 2.3	0.179	48
P8CD100-pH 2	616	0.394	2.0 and 2.3 and 5.2	0.175	44
P16CD100-pH 2	698	0.446	2.0 and 2.3 and 5.2	0.188	42
P30CD100-pH 2	656	0.454	2.0 and 2.3 and 5.2	0.145	32

S_{BET} = BET specific surface area determined in the relative pressure range 0.1–0.25, V_{cum}, PS = cumulative pore volume and pore size resulting from non-local density functional theory (NLDFT) calculations, V_{micro} = micropore volume determined from t-plot, % micro = (V_{micro}/V_{cum})*100. Reprinted with permission of the Royal Society of Chemistry from (Bleta et al. 2014c)

poly*pseudo*rotaxanes, as well as (iii) larger mesopores (5.8 nm) attributed to the columnar α-CD crystallites formed by the self-assembly of poly*pseudo*rotaxanes at their CD-rich segments. Therefore, various self-assembled motifs exist within the hydrogel network including naked PEG chains, poly*pseudo*rotaxanes and nanocrystallites. Moreover, nanocrystallites were found to gradually grow in size as the solution was loaded with more PEG and as the hydrogel network became denser. On the other hand, all materials prepared at pH 2 contained a high portion of micropores (1.8 nm) and small mesopores (2 nm), even at a high PEG concentration (30 mg mL^{-1}) (Table 3.1) indicating that, under more acidic conditions, a higher portion of unthreaded α-CD and uncovered PEG segments is available, thus leading to lower crosslinking densities within the hydrogel network.

Interestingly, the small angle X-ray scattering (SAXS) data (Fig. 3.9B) indicated the presence of two reflection peaks at $2\theta = 1.51°$ and 2.65° (q ratios $1:\sqrt{3}$), corresponding to d-spacing values of 5.84 nm and 3.33 nm, respectively, which can be indexed to the (100) and (110) Bragg reflections of a hexagonal mesostructured material. This means that some local order exists within these silica replicas, due to the self-assembly of poly*pseudo*rotaxanes in rather regular columnar bundles within the crystallites.

Representative TEM images of the silica replicas prepared at pH 4 with 30 mg mL^{-1} PEG showed the presence long tubular structures with 30–170 nm diameters (Fig. 3.10 a–c) made-up of several linear strings associated with the bundles of poly*pseudo*rotaxanes. Moreover, some local order can be noticed in the mesoporous network (Fig. 3.10 d), in agreement with the SAXS pattern. On the other hand, sharper striations were formed in the silicified hydrogel at pH 2 (Fig. 3.10 e and f). The mesoporous network was characterized by the presence of regular lattice fringes

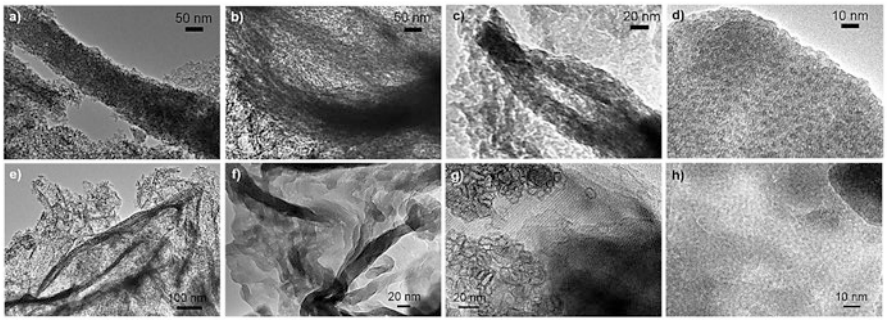

Fig. 3.10 Transmission electron microscopy (TEM) images of the calcined silica materials prepared from PEG (30 mg mL^{-1})/ α-CD (100 mg mL^{-1}) hydrogels at pH 4 (**a-d**) and pH 2 (**e-h**). Note the presence of long tubular structures with 30–170 nm diameters associated with the bundles of poly*pseudo*rotaxanes. Reprinted with permission of the Royal Society of Chemistry from (Bleta et al. 2014c)

(Fig. 3.10 g) consistent with a higher degree of structuration, as evidenced by SAXS. Worm-like pores with diameters of approximately 5 nm, represented by the bright points, were also observed (Fig. 3.10 h) in a relatively good agreement with the pore sizes previously determined by N_2-adsorption measurements.

These results demonstrated that the threading of α-CD onto PEG chains and the resulting nanocrystallites are affected by the pH of the aqueous solution. A schematic comparison of the replication process that occurs in PEG and PEG/α-CD systems at pH 4 and 2 is shown in Fig. 3.11. Depending on the pH of the hydrogel, several domains with various crosslinking densities can be formed within the organic templates giving rise to a wide range of pore sizes within the silica scaffolds. Therefore, in the case of the hydrogel prepared at pH 2, the presence of an excess of H_3O^+ ions may induce a protonation of the polymer -OH groups resulting in a lower degree of α-CD threading and a higher portion of naked polymer chains. The low level of α-CD threading onto PEG can explain the formation of less dense nanocrystallites within the hydrogel network. On the contrary, at pH 4, the higher concentration of threaded α-CD resulted in the formation of larger and denser nanocrystallites. Such differences in the supramolecular organization of PEG/α-CD assemblies may explain the higher degree of microporosity observed for materials prepared at pH 2 and the higher amount of large mesopores with a reduced degree of microporosity generated at pH 4. Thus, for instance, the silica material prepared with 30 mg mL^{-1} PEG and 100 mg mL^{-1} α-CD at pH 4 had a pore volume as high as 0.979 cm^3 g^{-1} and contained only 2.7% micropores, whereas the one prepared with the same amount of organics at pH 2 had a pore volume of 0.454 cm^3 g^{-1}, less than half that obtained at pH 4, and contains as much as 32% micropores (Table 3.1).

The explanation for the observed difference in porosity relies on the pH-induced structural changes that occur in the crosslinking densities of the nanocrystallites within the hydrogel network. Considering the low level threading of α-CD at pH 2 and the small size of the resulting nanocrystallites, materials with well-defined

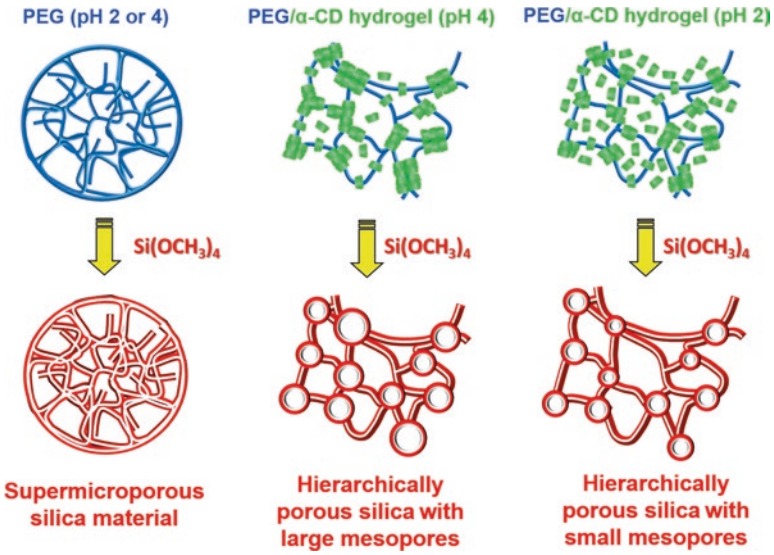

Fig. 3.11 Schematic illustration of the formation of hierarchical porous silica materials from PEG and PEG/α-CD hydrogels at pH 4 and pH 2. The crosslinking density of the nanocrystallites is enhanced with increasing pH from 2 to 4 yielding hierarchically porous silica with large mesopores (4–10 nm). Reprinted with permission of the Royal Society of Chemistry from (Bleta et al. 2014c)

small mesopores can be produced due to the lower, but better-controlled dispersion of the nanocrystallites within the hydrogel. On the other hand, the formation of large mesopores appears to be more favorable under mild acidic conditions (pH 4) due to the higher overall crystallinity of these hydrogels.

3.4 Main Strategies Toward the Synthesis Non-siliceous Mesoporous Oxides

3.4.1 The Template-Directed Colloidal Self-Assembly Approach

Non siliceous mesoporous metal oxides such as TiO_2 and Al_2O_3 are very difficult to prepare *via* a direct templating approach (*i.e.* using the cooperative self-assembly or the true liquid-crystal-phase templating (TLCT) processes, Fig. 3.3). Indeed, compared to silicon alkoxides, the hydrolysis and condensation of transition metal alkoxides are not easy to control precisely in aqueous phase. The resulting materials are generally not robust enough to maintain the mesostructure after the formation of the oxide framework, and they usually exhibit very poor crystallinity and low thermal stability after the template removal (Van Der Voort et al. 2008).

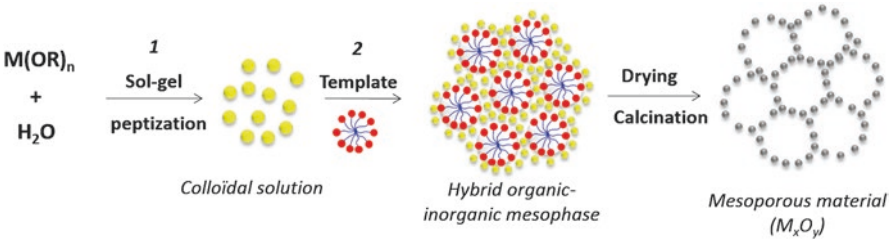

Fig. 3.12 Schematic illustration of the template-directed colloidal self-assembly approach were the colloidal nanoparticles act as building blocks for the construction of the inorganic network around the supramolecular template. Reprinted with permission from (Bleta et al. 2013). Copyright 2013 American Chemical Society

A versatile strategy to overcome the limitations of the cooperative self-assembly or the TLCT processes, and extend the scope of nanostructured porous materials beyond silica, is the so-called template-directed colloidal self-assembly approach (or the nanoparticle route) (Bleta et al. 2010). This approach involves the use of pre-synthesized colloidal particles which have the ability to self-assemble around a soft template (e.g., block copolymer or biopolymer). After drying and calcination, the recovered mesoporous materials are usually robust and present high surface areas, large pore volumes and tunable porosities (Bleta et al. 2010, 2012) (Fig. 3.12). Nanoparticles can be held together either by weak noncovalent forces, such as hydrogen bonding (Boal et al. 2000; Hao and Lian 2000) or by strong covalent bonds *via* different functional groups that can be fixed onto the nanoparticle surface (Patolsky et al. 2002; Lu et al. 2003). So far, the template-directed colloidal self-assembly has been successfully employed for the preparation of a variety of inorganic materials, especially semiconductor metal oxide nanoparticles, with various morphologies that depend on the characteristics of both the template and the colloidal nanocrystals (Yu and Peng 2002; Rajh et al. 1993).

3.4.2 Mesoporous Transition Metal Oxides from RaMeβ-CD/ Pluronic P123 Assemblies

3.4.2.1 Interactions between RaMeβ-CD and Pluronic P123

Before using the cyclodextrin/polymer assemblies as template, it is necessary to study their interactions in aqueous phase. Since the pioneering work of Harada *et al.* (Harada and Kamachi 1990) who showed that α-CD can form inclusion complexes with poly(ethylene glycol) (PEG) in aqueous solution to give poly*pseudo*rotaxanes with a necklace-like structure, a range of polymeric guests have been found to form inclusion complexes with cyclodextrins (Harada 1996). However, compared to the native CDs, the interactions between the modified CDs and polymers have been less investigated in the literature. The results reported by

Gaitano et al. (1997), and later supported by other authors (Joseph et al. 2007; Lazzara and Milioto 2008; Nogueiras-Nieto et al. 2009; Dreiss et al. 2009; Tsai et al. 2010), showed that, similarly to native β-CD, the macrocycle of a dimethylated β-CD is able to complex the hydrophobic poly(propylene oxide) blocks of different nonionic triblock copolymers of the poly(ethylene oxide) (PEO)-b-poly(propylene oxide) (PPO)-b-poly(ethylene oxide) (PEO) (*i.e.* Pluronics). On the other hand, spectroscopic and time-resolved small angle neutron scattering measurements performed on mixtures of heptakis (2,6-di-o-methyl)-β-CD and three Pluronics [P123 ($PEO_{20}PPO_{70}PEO_{20}$), P85 ($PEO_{39}PPO_{52}PEO_{39}$) and F127 ($PEO_{107}PPO_{70}$ PEO_{107})] evidenced that the micellar rupture occurs with extremely fast kinetics, thus excluding the possibility of poly*pseudo*rotaxane formation *via* inclusion complexation (Valero et al. 2012). Interestingly, in the case of Pluronic P123, the authors reported a possible restructuration of the micelles toward swollen lamella, with an interlayer spacing that was much higher than the typical values reported in literature with conventional swelling agents (Holmqvist et al. 1998). However, the phenomenon of micellar rupture was shown to be highly sensitive to the substitution degree, nature and position of the modified groups within the cyclodextrin (Joseph et al. 2007; Valero et al. 2012). Thus, in contrast to the micellar rupture observed with the heptakis (2,6-di-o-methyl)-β-CD, micelles remained intact in the presence of other substituted β-cyclodextrin derivatives, such as the 2,3,6-trimethyl-β-CD, 2-hydroxyethyl-β-CD and 2-hydroxypropyl-β-CD (Valero et al. 2012).

The supramolecular assemblies formed between the Pluronic P123 ($PEO_{20}PPO_{70}PEO_{20}$) and the randomly methylated β-cyclodextrin (RaMe β-CD) were investigated with the attempt to be used as templates for the synthesis of porous inorganic solids (Bleta et al. 2013; 2014b). The RaMeβ-CD where methylation occurs at the C2, C3 or C6 positions with statistically 1.8 OH groups modified per glucopyranose unit, can be seen as a versatile structure directing agent. Indeed, this cyclodextrin is highly soluble in water, cheap, non-toxic, commercially available (Uekama and Irie 1987) and surface active (Leclercq et al. 2007). To investigate whether RaMeβ-CD has an impact on the copolymer micellar growth, dynamic light scattering (DLS) measurements were performed at 25 °C. Figure 3.13 a,b displays the DLS plots of the aqueous solutions prepared with 7.8 wt. % P123 and increasing amounts of RaMeβ-CD. In the range of 5–15 mg mL^{-1} RaMeβ-CD, the hydrodynamic radius remained constant (R_H = 9.1 nm), but the scattering intensity increased. This result was explained by the preferential location of these oligosaccharides in the water-rich corona of the P123 micelles, where they preferentially interact with the hydrophilic PEO blocks of the copolymer by hydrogen bonding. In contrast, for higher RaMeβ-CD concentrations, the size distribution plots indicated a progressive increase in the micellar hydrodynamic radius from 9.1 to 15.5 nm when the RaMeβ-CD concentration increased from 30 to 80 mg mL^{-1} (Fig. 3.13 b). Such variation was attributed to the ability of this cyclodextrin to act as swelling agent for the P123 micelles. Indeed, RaMeβ-CD with an average degree of substitution (DS) of about 12.6 tends to be more lipophilic than the native β-CD, showing a higher affinity for the hydrophobic core of the block copolymer micelles. Therefore,

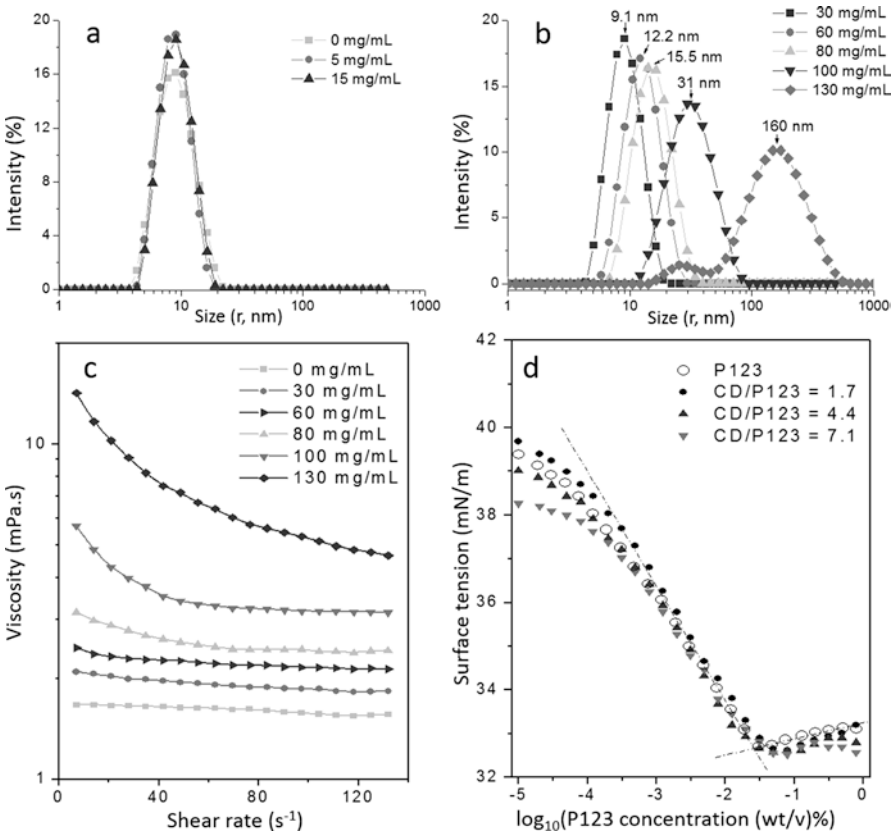

Fig. 3.13 Dynamic light scattering data (**a, b**), apparent viscosity *vs.* shear rate curves (**c**) and surface tension plots (**d**) of Pluronic P123 solutions prepared with various amounts of RaMeβ-CD. All measurements were performed at 25 °C. Adapted with permission from (Bleta et al. 2013). Copyright 2013 American Chemical Society

it was assumed that, in this concentration range, additional hydrophobic interactions occur between the OCH_3 groups of the cyclodextrin and the PPO blocks of the copolymer, resulting in the preferential location of RaMeβ-CD at the PPO-PEO interface layer. The scattering intensity of these assemblies gradually decreased with the CD concentration due to the formation of less well-defined objects with more flexible interfaces. A remarkable increase in the growth of these assemblies was noticed upon addition of larger amounts of RaMeβ-CD. Thus, the hydrodynamic radius abruptly shifted to 31 nm and 160 nm for 100 mg mL^{-1} and 130 mg mL^{-1} RaMeβ-CD respectively. These values far exceed the dimension of the P123 micelles even when the PEO and PPO chains are in a fully extended conformation, thus suggesting modification of the interfacial curvature of the RaMeβ-CD-loaded micelles and a shape transformation from spherical to ellipsoidal. Such shape trans-

formation was found to occur for RaMeβ-CD/P123 molar ratios higher than 7.5 (Bleta et al. 2014b).

The viscosity of the RaMeβ-CD-loaded micelles was also measured. Figure 3.13c shows the apparent viscosity *vs.* shear rate plots recorded at 25 °C. The addition of 30 and 60 mg mL^{-1} RaMeβ-CD induced no significant modification of the rheological behavior of the micellar solutions since the apparent viscosity remained nearly constant (∼1.6–2.2 mPa·s) over the entire range of shear rates (0–130 s^{-1}). Conversely, the addition of 80 and 100 mg mL^{-1} RaMeβ-CD induced a shear-thinning behavior (*i.e.*, the viscosity decreased with increasing the shear rate), as well as a more pronounced increase in viscosity to ∼2.4 and ∼3.2 mPa·s, respectively, as measured at 130 s^{-1}. Such a particular rheological behavior is usually observed in thixotropic systems comprised of particles with strong shape anisotropy such as rods, discs or platelet shapes (Bleta et al. 2011). This behavior was therefore consistent with the formation of ellipsoidal structures, in agreement with the DLS data.

Finally information about the impact of RaMeβ-CD on the micellization of Pluronic P123 was provided by surface tension measurements. If the hydrophobic interactions between the PPO chains, which are the driving force for the micellization, are screened by the presence of the cyclodextrin, this may lead to a disruption of the copolymer micelles and an increase of the Critical Micelle Concentration (CMC) (Bernat et al. 2008; Mahata et al. 2010). Figure 3.13 d shows the surface tension plots recorded at 25 °C for Pluronic P123 solutions prepared without and with RaMeβ-CD (CD/P123 molar ratios in the range of 1.7–7.1). The surface tension of the copolymer was not significantly affected by the addition of RaMeβ-CD whatever the molar ratio of RaMeβ-CD to P123 used, giving further evidence that the interactions between Pluronic and RaMeβ-CD are relatively weak and do not affect significantly the micellization process.

3.4.2.2 Mesoporous γ-Al_2O_3 Materials with Tunable Porosity

When these supramolecular coassemblies were utilized as templates, mesoporous γ-alumina (γ-Al_2O_3) with a crystalline framework, large pore size and high surface area were obtained (Bleta et al. 2013). The synthetic procedure is schematized in Fig. 3.14. Briefly, in a first step, boehmite nanoparticles were synthesized in aqueous solution (H_2O/Al ≈ 100) using aluminum tri-sec-butoxide $Al(OBu)_3$ (denoted ASB) and nitric acid as the metal oxide precursor and peptizing agent (HNO_3/Al = 0.07), respectively. In a second step, boehmite nanoparticles were allowed to self-assemble around the RaMeβ-CD/P123 assemblies at room temperature. The P123 concentration was fixed at 7.8% (PEO/Al = 1) whereas the RaMeβ-CD concentration was varied from 30 to 130 mg mL^{-1} (*i.e.* RaMeβ-CD/P123 molar ratio in the range of 1.7 to 7.1). After drying at 60 °C for 48 h, xerogels were calcined at 500 °C to remove the organic template and allow the transition from boehmite (AlO(OH)) to γ-Al_2O_3, which is assumed to occur at ∼380 °C, as evidenced by thermal analysis and confirmed by XRD measurements.

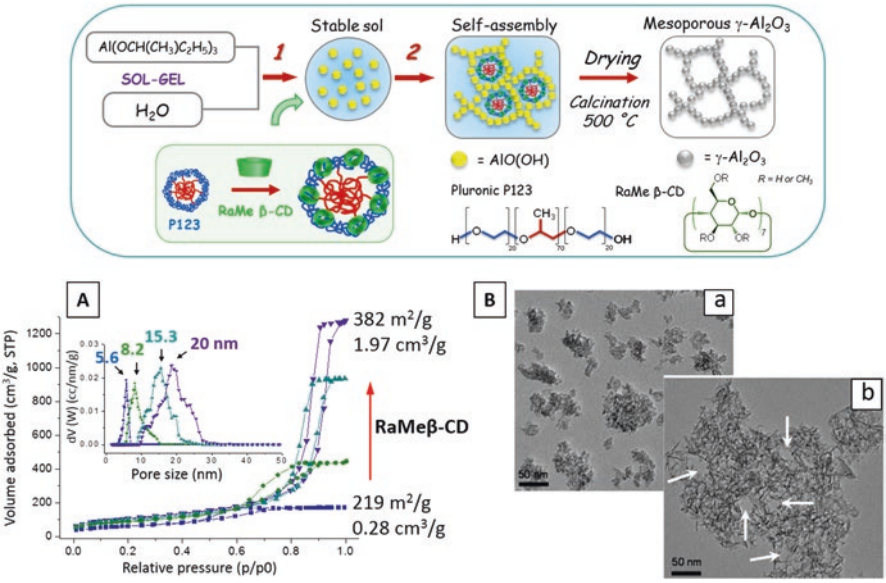

Fig. 3.14 Top: Schematic illustration of the template-directed synthesis of mesoporous γ-Al_2O_3 with controlled porosity where boehmite (AlO(OH)) colloids act as building blocks for the construction of the inorganic network. (A) N_2-adsorption isotherms and corresponding pore size distributions (inset) for the mesoporous γ-Al_2O_3 prepared without template, with Pluronic P123 (PEO/Al = 1) and with increasing amounts of RaMeβ-CD (30–130 mg mL^{-1}). Note that the pore size can be adjusted from 5.6 to 20 nm by addition of RaMeβ-CD to the micellar solution of Pluronic. (B) Transmission electron microscopy (TEM) images for mesoporous γ-Al_2O_3 prepared without template (**a**) and with RaMeβ-CD-loaded micelles (80 mg mL^{-1}) (**b**). Adapted with permission from (Bleta et al. 2013). Copyright 2013 American Chemical Society

To obtain information about the textural characteristics of the calcined γ-Al_2O_3, N_2 adsorption-desorption analyses were carried out. From Fig. 3.14a, it can be seen that all isotherms presented a distinct H1 hysteresis loop characteristic of mesoporous materials. The control sample, prepared without template, presented a capillary condensation step that started at a relative pressure (P/P_0) of about 0.4 indicating the presence of small mesopores. The corresponding pore size distribution (PSD) plot was relatively narrow and centered at 5.6 nm. The formation of such small pores was attributed to the assembly of several crystallites in compact rearrangements with "card-pack" microstructures. Upon addition of the block copolymer (P1-Al-T500 sample), a steep rise in the nitrogen uptake was observed at relative pressures (P/P_0) higher than 0.8 indicating the formation of large mesopores. Accordingly, the corresponding pore size distribution plot indicated a dramatic increase in the pore size (from 5.6 to 14.8 nm) and pore volume (from 0.28 to 1.37 $cm^3\ g^{-1}$) due to the formation of big micelles acting as soft templates. Notably, the textural characteristics were further improved upon addition of increasing amounts of RaMeβ-CD. Thus, the pore size increased from 14.8 to 19.7 nm and the pore volume from 1.45 to 1.97 $cm^3\ g^{-1}$ (Table 3.2). The most striking textural

Table 3.2 Textural characteristics of mesoporous γ-Al_2O_3 calcined at 500 °C

Sample	S_{BET}(m^2 g^{-1})	PV(cm^3 g^{-1})	S_{cum}(m^2 g^{-1})	V_{cum}(cm^3 g^{-1})	PS(nm)
Al-T500	219	0.28	227	0.26	5.6
P1-Al-T500	357	1.37	387	1.35	14.8
P1-CD30-Al-T500	354	1.45	387	1.43	14.9
P1-CD60-Al-T500	356	1.62	372	1.60	16.3
P1-CD80-Al-T500	382	1.97	427	1.94	19.3
P1-CD130-Al-T500	360	1.66	373	1.63	10.5 and 19.7

P = [PEO]/[Al], CD = RaMeβ-CD concentration in the sol (mg mL^{-1}), T = calcination temperature, S_{BET} = BET specific surface area determined in the relative pressure range 0.1–0.25, PV = pore volume calculated from adsorbed volume at $P/P_o = 0.995$, S_{cum}, V_{cum}, PS = cumulative surface area, cumulative volume and pore size resulting from non-local density functional theory (NLDFT) calculations. Reprinted with permission from (Bleta et al. 2013). Copyright 2013 American Chemical Society

characteristics were obtained for the material prepared with 80 mg mL^{-1} RaMeβ-CD (average pore size = 19.3 nm, pore volume = 1.97 cm^3 g^{-1} and specific surface area = 382 m^2 g^{-1}). Such an enhancement in the porosity can be directly attributed to the swelling effect of RaMeβ-CD, in line with the trend observed from DLS data.

The representative transmission electron microscopy (TEM) images (Fig. 3.14b) indicated that contrary to the non-templated alumina which was globally dense and made of aggregated particles, the templated material showed a well-defined fiberlike morphology, indicating the important role of the template in restructuring the particle network. Interestingly, in addition to the fiberlike morphology, several voids with an average diameter of ~20 nm, similar to the pore size determined from N_2-adsorption measurements, were also present at a very high yield throughout the nanoparticle network (see arrows). These results indicated that, after the thermal treatment at 500 °C, the material successfully adopted some characteristics of the supramolecular template. Hence, the void space formed between the nanoparticles may be seen as a solid replica of the original swollen micelles formed by the coassembly of the copolymer and the cyclodextrin.

3.4.2.3 Mesoporous TiO_2 Materials with Tunable Porosity and Crystallinity

The template-directed colloidal self-assembly approach was successfully extended to the synthesis of mesoporous titanium dioxide (TiO_2, titania) (Lannoy et al. 2014; Bleta et al. 2014a, b, c). TiO_2 has been applied as one of the most promising photocatalysts for the removal of industrial organic pollutants from water and air (Zhao et al. 2004; Gomathi Devi and Kavitha 2013), as well as for the photocatalytic water splitting for hydrogen production (Fujishima and Honda 1972). TiO_2 commonly crystallizes in three polymorphic forms, *i.e.* anatase (tetragonal, I41/amd), brookite (orthorhombic, Pbca) and rutile (tetragonal, P42/mnm). Bulk rutile is the only

thermodynamically stable phase, while bulk anatase and bulk brookite are metastable (Zhang and Banfield 1998, 2000). Nevertheless, under controlled conditions, anatase and brookite can be thermodynamically stabilized when the particle size is below 11 nm for the former and between 11 and 35 nm for the latter (Zhang and Banfield 2000). Among the three polymorphs, anatase and rutile have received the greatest attention due to the facility of their synthesis. Anatase has a band gap of 3.2 eV with the absorption edge at 386 nm which lies in the near UV range, whereas rutile has a lower band gap of 3.02 eV with the adsorption edge in the visible range at 416 nm. The anatase polymorph is usually reported to be more active than rutile (Pillai et al. 2007), mainly because of the fast electron-hole recombination in the latter which results from its lower band gap (Periyat et al. 2008).

It is today well-accepted that the photocatalytic reactions mainly take place on the surface of the irradiated semiconductor (Linsebigler et al. 1995). Consequently, in addition to the effect of the crystal phase composition mentioned above, other factors such as the crystallite size, the surface area, the pore volume, the orientation of the active faces and the adsorption properties of the pollutant are also likely to affect the photocatalytic activity (Ovenstone 2001; Yang et al. 2008; Chen and Caruso 2013; Nursam et al. 2015; Wang et al. 2013). Therefore, the impact of the RaMeβ-CD-P123 micelles on the structural, textural and morphological characteristics of titania was investigated. In a first step, a translucent hydrosol made-up of crystalline TiO_2 nanoparticles was synthesized in water/isopropanol solution (H_2O/Ti = 88) by a sol-gel method using titanium isopropoxide ($Ti(OiPr)_4$) as inorganic precursor and nitric acid as peptizing agent (HNO_3/Ti = 0.2). In a second step, the RaMeβ-CD-P123 supramolecular assemblies were used as templates to direct the self-assembly of the pre-synthesized TiO_2 nanoparticles (Fig. 3.15). This second step of synthesis was performed at 25 °C because at this temperature, the RaMeβ-CD-P123 solutions present the lowest viscosity, which facilitates the structuration of the nanoparticles around the supramolecular template. After drying, the recovered xerogels were calcined at 500 °C to remove the template and allow further crystallization of the material.

To gain information about the impact of the template on the textural characteristics of titania, N_2-adsorption analyses were performed. All calcined samples display type IV isotherms which are typical features of mesoporous materials (Fig. 3.15A). The control sol-gel titania presented a capillary condensation step that started at a relative pressure (P/P_0) of about 0.4, indicating the presence of small mesopores with a diameter of 5.3 nm ascribed to the holes formed between the close packed crystallites. The addition of copolymer (P27 sample) strongly, but predictably, improved the textural characteristics of the material, showing an abrupt increase of the pore size to 9.2 nm (Table 3.3). Interestingly, when the cyclodextrin was added to the block copolymer solution, the textural characteristics were further improved. Therefore, for RaMeβ-CD/Ti molar ratios comprised between 0.046 and 0.198, the pore size increased progressively from 9.4 to 12.1 nm and the pore volume from 0.25 to 0.35 $cm^3\ g^{-1}$. No notable evolution occurred for RaMeβ-CD/Ti molar ratios higher than 0.198 (Table 3.3) for which the isotherms became quite different in the

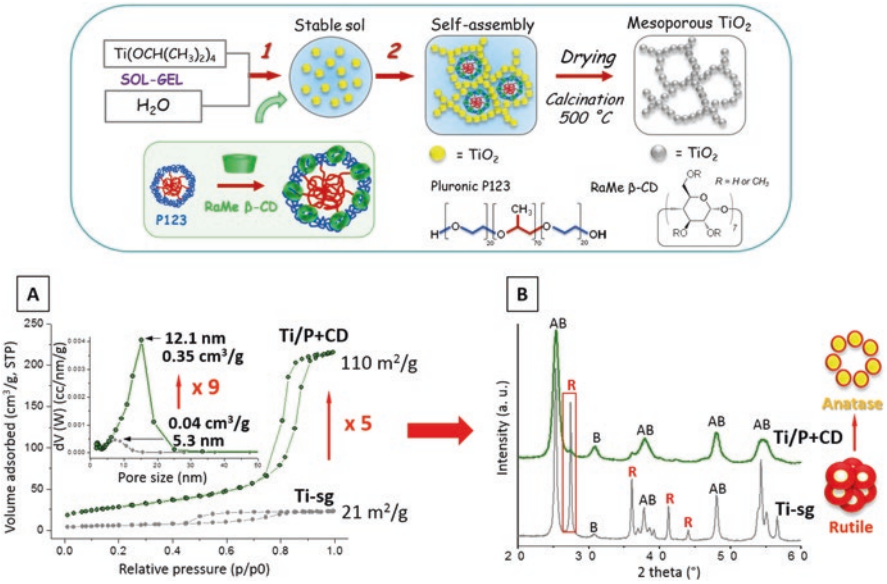

Fig. 3.15 Top: Schematic illustration of the template-directed synthesis of mesoporous crystalline titania where TiO_2 colloids act as building blocks for the construction of a nanostructured framework around the organic template. (**A**) N_2 adsorption isotherms and pore size distributions (inset) for the sol-gel TiO_2 prepared without template, and nanostructured TiO_2 prepared with RaMeβ-CD-P123 assemblies. (**B**) X-ray diffraction (XRD) patterns of the corresponding materials. "A", "B" and "R" denote the anatase, brookite and rutile phases respectively. Adapted with permission of the Royal Society of Chemistry from (Lannoy et al. 2014)

region of relative pressures higher than 0.9 where the N_2 adsorption continued to increase, indicating also the presence of some macropores.

Before any thermal treatment, the sol-gel TiO_2 contained 68% anatase (A) (JCPDS card no. 00–021-1272) and 32% brookite (B) (JCPDS card no. 01–076-1934). The crystallite sizes determined from the Scherrer formula were 6.6 ± 0.8 nm (A) and 5.3 ± 0.6 nm (B). Such a small particle size was explained by the high hydrolysis ratio employed which favors fast nucleation rates producing small and well-crystallized nanoparticles. However, upon calcination at 500 °C, the small particles agglomerated and the increased degree of nanoparticle packing facilitated the phase transformation. Therefore, from the diffraction diagram of the control sol-gel TiO_2 (Fig. 3.15B), one can note the appearance of an intense sharp peak at $2\theta = 27.4°$ corresponding to the (110) plane of the rutile (R) (JCPDS card no. 00–034-0180), arising from the transformation of both anatase and brookite during calcination. The contents of anatase and brookite, determined from the Rietveld refinement, dropped to ~35% and ~27% respectively, while ~38% rutile formed as a result of the sintering (Table 3.3). Meanwhile, the size of these three polymorphs grew to 36 nm (A), 19 nm (B) and 60 nm (R) as the phase transformation progressed. When the Pluronic alone was utilized as template (P27 sample), the rutile reflections

Table 3.3 Structural and textural characteristics of the different mesoporous TiO_2 prepared through template-directed colloidal self-assembly

Sample			Anatase		Brookite		Rutile		N_2 adsorption		
			cs[c] (nm)	ct[d] (%)	cs[c] (nm)	ct[d] (%)	cs[c] (nm)	ct[d] (%)	S_{BET}[e] ($m^2\ g^{-1}$)	pv[f] ($cm^3\ g^{-1}$)	ps[g] (nm)
	P + RB/Ti[a]	RB/P[b]	Effect of addition of P123-RaMeβ-CD assemblies								
Sol-gel TiO_2	–		36.4±2.9	35.3±2.8	18.7±1.5	26.5±2.1	60.4±4.8	38.2±3.1	21±1	0.03±0.00	5.3±1.1
P27	0.027	0	17.2±1.4	54.5±4.4	13.8±1.1	42.1±3.4	20.8±1.7	3.4±0.3	89±4	0.24±0.01	9.2±1.8
P27RB46	0.073	1.7	15.5±1.2	51.5±4.1	11.6±0.9	46.0±3.7	16.6±1.3	2.5±0.2	109±5	0.25±0.01	9.4±1.9
P27RB122	0.149	4.5	13.6±1.1	50.1±4.0	8.9±0.7	48.6±3.9	13.4±1.1	1.3±0.1	112±6	0.29±0.01	10.3±2.1
P27RB198	0.225	7.4	10.8±0.9	47.7±3.8	7.6±0.6	51.5±4.1	10.7±0.9	0.8±0.1	110±6	0.35±0.02	12.1±2.4
P27RB305	0.332	11.4	9.9±0.8	45.4±3.6	6.7±0.5	54.3±4.3	9.0±0.7	0.3±0.1	96±5	0.36±0.02	12.4±2.5
			Effect of the calcination temperature (P27RB198 sample)								
T400	0.225	7.4	9.0±0.7	90.4±7.2	4.4±0.4	9.6±0.8	–	–	158±8	0.45±0.02	9.3±1.9
T500	0.225	7.4	10.8±0.9	47.7±3.8	7.6±0.6	51.5±4.1	10.7±0.9	0.8±0.1	110±6	0.35±0.02	12.1±2.4
T600	0.225	7.4	17.7±1.4	48.1±3.8	8.5±0.7	35.2±2.8	23.6±1.9	16.7±1.3	58±3	0.35±0.02	21.0±4.2
T700	0.225	7.4	35.2±2.8	37.6±3.0	–	–	62.5±5.0	62.4±5.0	16±1	0.14±0.01	–
T800	0.225	7.4	–	–	–	–	82.8±6.6	100	–	–	–

[a](Pluronic P123 + RaMeβ-CD)/Ti molar ratio in the sol, [b]RaMeβ-CD/P123 molar ratio in the sol, [c]crystallite size calculated from the Scherrer formula, [d]polymorph content determined from Rietveld refinements, [e]specific surface area determined by BET method in the relative pressure range of 0.1–0.25, [f]pore volume computed by non-local density functional theory (NLDFT) calculations, [g]pore size determined by NLDFT. Reprinted with permission of the Royal Society of Chemistry from (Lannoy et al. 2014)

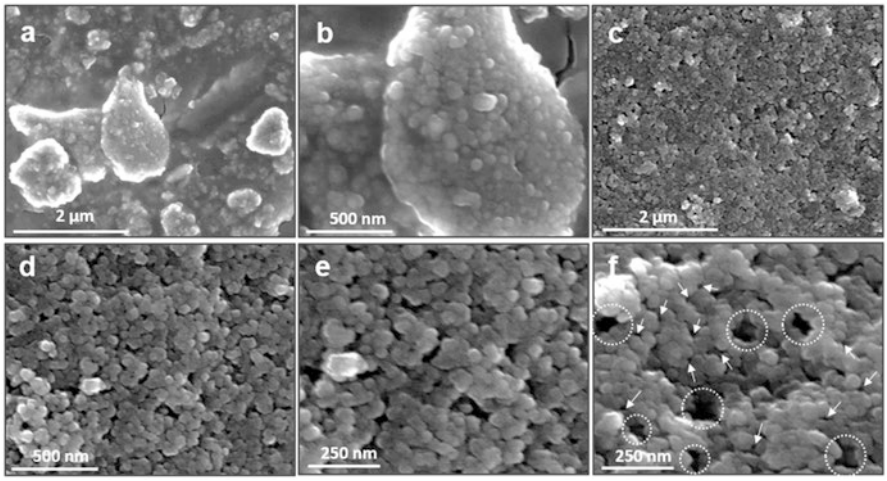

Fig. 3.16 Representative field emission scanning electron microscopy (FE-SEM) images taken at different magnifications for sol-gel titania prepared without template (a and b) and with P123-RaMeβ-CD assemblies (P27RB198 sample) (c-f). Note the presence of mesopores with an average diameter of 10–20 nm (see arrows) and macropores with an average diameter of 60–100 nm (see dotted circles). Reprinted with permission of the Royal Society of Chemistry from (Lannoy et al. 2014)

remarkably decreased in intensity indicating a delay in the phase transformation. Interestingly, this phenomenon became even more pronounced upon addition of increasing amounts of RaMeβ-CD. Indeed, the diffraction peaks of anatase and brookite became broader indicating smaller crystallites, while more brookite formed and rutile polymorph almost disappeared. Thus, for the sample prepared with a CD/Ti molar ratio of 0.198, the size of the crystallites decreased to 8–11 nm and the rutile content became negligible with respect to the contents of anatase (48%) and brookite (52%).

From the representative FE-SEM images of the materials prepared without and with template (Fig. 3.16), the effect of the supramolecular assemblies on the morphology of the network was clearly visualized. Therefore, the sol-gel titania prepared without template was comprised of rounded particles densely packed into large aggregates with no regular shape and very low interparticle porosity (Fig. 3.16a and b). In contrast, the material prepared using the supramolecular assemblies (P27RB198 sample) showed uniform particles with spherical shape indicating the important role of the template in restructuring the particle network (Fig. 3.16c-f). Moreover, several mesopores were also noticed at a high yield with an average diameter of 10–20 nm (see arrows) as well as some macropores with an average diameter of 60–100 nm (see dotted circles), in accordance with the shape of the N_2-adsorption isotherm at high relative pressures. This indicated that the material had adopted some characteristics of the supramolecular template maintaining a nano-structured network even after calcination at 500 °C.

3.4.3 Mesoporous Nanocomposites from Cyclodextrins or RaMeβ-CD/Pluronic P123 Assemblies

3.4.3.1 Using Native and Modified Cyclodextrins as Structure Directing Agents

The binding affinity of cyclodextrin on titania nanoparticles is highly dependent on their nature, natives or modified. Thus, the adsorption isotherms have been shown to follow the Langmuir model, and adsorption capacities as high as 33 μmol g^{-1} were obtained with the native β-CD compared to 15.2 μmol g^{-1} with the permethylated 2-O-methyl-β-CD (DS = 4) and 0 μmol g^{-1} with the 2,6-di-O-methyl-β-CD (DS = 14) (Zhang et al. 2013). Such adsorption was proposed to occur predominantly through the -OH groups located at the secondary ring face of β-CD, which also caused the selective photodegradation of a series of bisphenols by preferential inclusion complexation with the primary ring side.

In the case of the native α-CD, β-CD and γ-CD, the numerous hydroxyl groups, located on both the narrow and the wider ring faces, may favor the interaction of the macrocycle with the surface -OH groups of titania. Conversely, the 2-hydroxypropyl β-CD (HPβ-CD) and the randomly methylated β-CD (RaMeβ-CD), possessing less surface hydroxyl groups on the ring, are likely to form less hydrogen bonds. Additionally, the adsorption capacity of these modified oligosaccharides may be hindered by the steric constraint created by the 2-hydroxyproyl and methoxy groups, thus leaving less place for the interaction with the non-substituted hydroxyl groups.

The changes occurring in the structure of cyclodextrin assemblies after interaction with titania colloids and after solvent evaporation were followed by XRD measurements. From Fig. 3.17, it can be seen that the native α-CD and β-CD, before being introduced to the titania hydrosol, present several sharp diffraction lines characteristic of their cage-type crystalline microstructure (Harada et al. 2009). After interaction with titania colloids, the disappearance of the most intense reflections observed at 12.2°, 14.3° and 21.6° with the neat α-CD and at 9.0° and 12.5° with the neat β-CD suggested the disruption of the cage-type microstructure due to the adsorption of these oligosaccharides on the titania surface. On the other hand, the neat β-CD derivatives (HPβ-CD and RaMeβ-CD) presented only two broad peaks due to their amorphous character. Interestingly, from the patterns of the hybrid HPβ-CD/TiO_2 and RaMeβ-CD/TiO_2 materials, it was noticed that these reflections were still intense, indicating weaker interactions with the titania surface. Similar results were obtained with carbon materials which presented a significantly lower adsorption capacity towards HPβ-CD and RaMeβ-CD compared to the native cyclodextrins, but a higher capacity to improve the dispersion of carbon particles in water (Okumura et al. 2001).

The substitution of hydroxyl groups by a relatively large number of methoxy (-OCH_3) or 2-hydroxypropyl (-$OCH_2CH(CH_3)OH$) groups is one of the main factors that affects the physicochemical properties of the cyclodextrins, implying changes in both the solubility profile (due to the disruption of intermolecular hydrogen

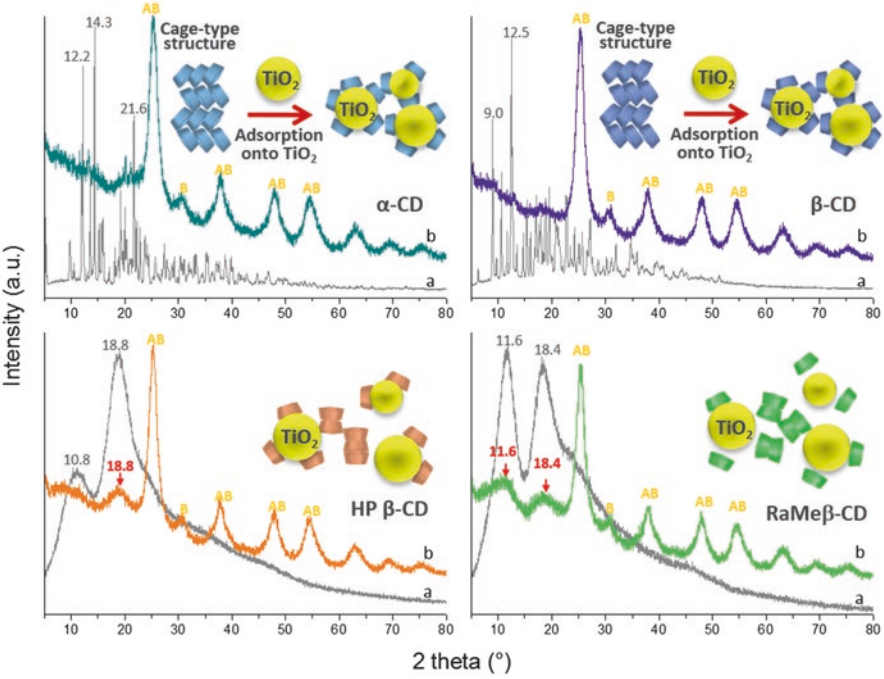

Fig. 3.17 X ray diffraction patterns of the neat cyclodextrins (a) and corresponding cyclodextrin/TiO_2 hybrid xerogels (b) prepared with aCD/Ti molar ratio of 0.076 for α-CD, HPβ-CD, and RaMeβ-CD and a molar ratio of 0.032 for β-CD. The xerogels were dried at 60 °C. Note that after interaction with titania colloids, the most intense reflections observed with the neat α-CD and β-CD disappear suggesting the disruption of the cage-type microstructure due to the adsorption of these cyclodextrins on the TiO_2 surface. Reprinted with permission from (Bleta et al. 2014a). Copyright 2014 American Chemical Society

bonds) and the interfacial behavior (due to the presence of more marked hydrophobic and hydrophilic microenvironments). Thus, the surface tension data shown in Fig. 3.18A indicate that, in contrast to the native cyclodextrins, which are almost not surface-actives, HPβ-CD and RaMeβ-CD present surface tension values of 59.9 and 56.8 mN m^{-1} respectively at 38 mM (concentration utilized for the preparation of the mesoporous titania materials). The slightly lower surface activity of HPβ-CD compared to RaMeβ-CD may be explained by the lower lipophilic character of the 2-hydroxypropyl groups compared to the methoxy ones. In this sense, the relatively higher surface activity of RaMeβ-CD may offer a means to reduce the surface energy of titania nanocrystals, thus facilitating their movement which is critical for their self-assembly. Significant modifications were also observed on the textural characteristics of the photocatalysts (Fig. 3.18B). Thus, using α-CD, the specific surface area increased from 21 to 68 m^2 g^{-1}, the pore volume from 0.03 to 0.13 cm^3 g^{-1} and the pore size from 5.3 to 7.0 nm. Similar results were also obtained with β-CD and γ-CD. Interestingly, the porosity was further enhanced when the modified cyclodextrins were used as structure directing agents and the most relevant

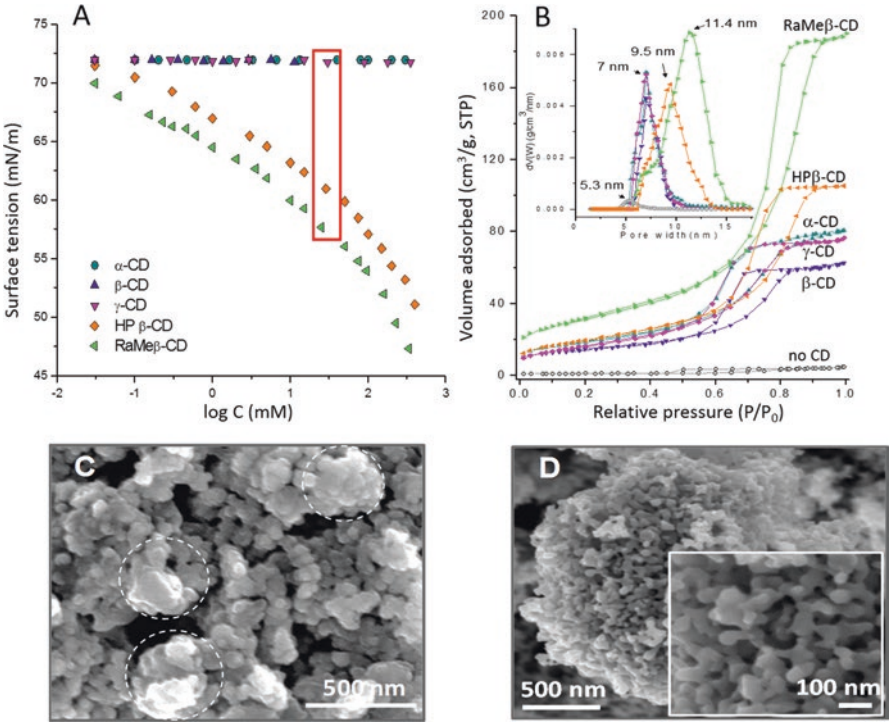

Fig. 3.18 (A) Surface tension plots of various cyclodextrins in water at 25 °C. The solid rectangle shows the domain of cyclodextrin concentrations under which TiO_2 materials have been prepared. (**B**) N_2-adsorption isotherms and corresponding pore size distributions (inset) of TiO_2 prepared without template and with various CDs. Representative field emission scanning electron microscopy (FE-SEM) images for sol-gel TiO_2 prepared with α-CD (C) and RaMeβ-CD (D). Note the formation of highly interconnected pore network with the methylated CD. Adapted with permission from (Bleta et al. 2014a). Copyright 2014 American Chemical Society

textural characteristics were obtained for titania prepared with RaMeβ-CD presenting a specific surface are of 115 $m^2\ g^{-1}$, a pore volume of 0.3 $cm^3\ g^{-1}$ and a pore size of 11.4 nm.

Moreover, from the representative field emission scanning electron microscopy (FE-SEM) images, it was noticed that the cyclodextrin had also an impact on the morphology of titania catalysts (Fig. 3.18C, D). Therefore, compared to native β-CD which produced some local agglomeration of the nanoparticles (see white circles in Fig. 3.18C), RaMeβ-CD gave rise to a highly interconnected pore network (Fig. 3.18D).

The overall picture emerging from these experimental data is that among the five cyclodextrins investigated, the RaMeβ-CD presents the best combination of surface active properties and weak CD-CD intermolecular interactions to efficiently direct the self-assembly of titania nanoparticles in a uniform network. The mechanism suggested for this self-assembly is shown in Fig. 3.19. In the presence of the native

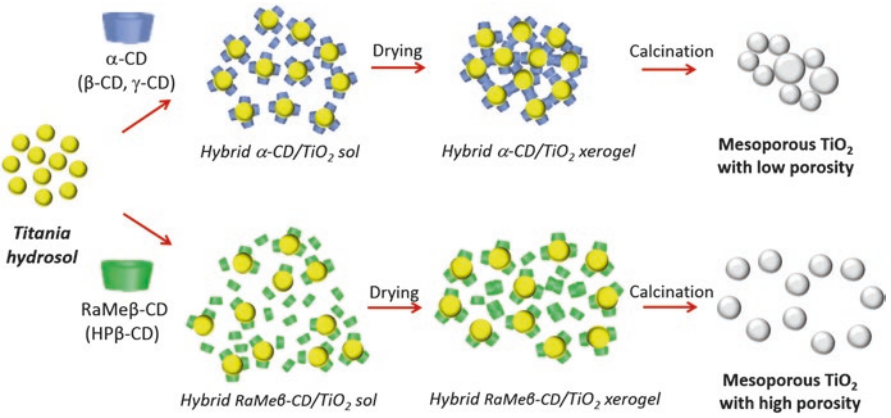

Fig. 3.19 Schematic illustration of the mechanism proposed for the self-assembly of titania colloids in the presence of native cyclodextrins (α-CD, β-CD, and γ-CD) and modified cyclodextrins (RaMeβ-CD and HPβ-CD). Reprinted with permission from (Bleta et al. 2014a). Copyright 2014 American Chemical Society

cyclodextrins (α-CD, β-CD and γ-CD), the colloid interface is rather rough (due to its high surface energy) and the intermolecular interactions are stronger (due to the numerous -OH groups). By consequence, the interactions between adsorbed cyclodextrins should favor the local agglomeration of titania nanoparticles during solvent evaporation, thus resulting in a less porous network. By contrast, in the presence of HPβ-CD and RaMeβ-CD, smoother interfaces are created by the lipophilic groups present in the macrocycle, leading to a decrease in the surface energy of titania nanocrystals and a reorganization of the colloids in a more homogeneous and porous network with small sizes and a fine morphology.

3.4.3.2 Mesoporous UV-Light Responsive TiO_2 Photocatalysts

To evaluate the photocatalytic activity of the titania materials prepared using the different cyclodextrins as structure directing agents, phenoxyacetic acid (PAA), a toxic herbicide, was chosen as probe molecule for degradation under UV light (360 nm). PAA is a parent molecule of the well-known 2,4-dichlorophenoxyacetic acid (2,4-D) and 2,4,5-trichlorophenoxyacetic acid (2,4,5-T) herbicides (Singh et al. 2007). The PAA photodegradation rates obtained with the different photocatalysts after 7 hours of exposure under UV-light illumination (360 nm) (Fig. 3.20) show that the nature of the cyclodextrin has an impact on the photocatalytic activity of titania. Thus, TiO_2 materials prepared from α-CD, β-CD and γ-CD were all photoactive under UV irradiation and gave a PAA degradation rate in the range of 58–64%, which was almost 45% higher than that of the sol-gel TiO_2 (43%). Further enhancement in the photocatalytic activity was noticed with the material prepared from HPβ-CD showing an intermediate PAA degradation rate of 72%

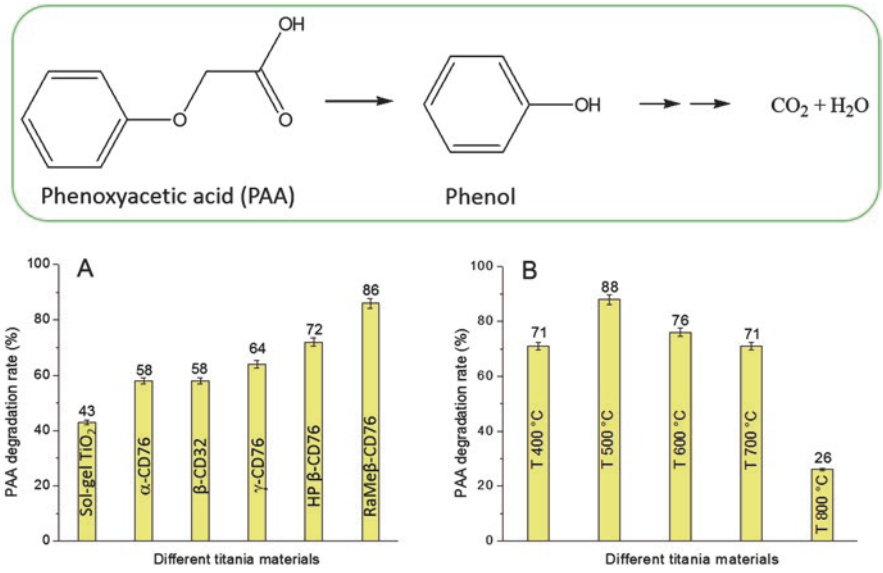

Fig. 3.20 Photocatalytic degradation rate of the phenoxyacetic acid (PAA) under UV-light irradiation after 7 h on titania materials prepared (**A**) with various cyclodextrins at a fixed CD/Ti molar ratio: 0.076 for α-CD, γ-CD, HPβ-CD, and RaMeβ-CD, and 0.032 for β-CD. Adapted with permission from (Bleta et al. 2014a). Copyright 2014 American Chemical Society. (**B**) Effect of calcination temperature on the photocatalytic activity of TiO_2 materials prepared from RaMeβ-CD/P123 assemblies. Adapted with permission of the Royal Society of Chemistry from (Lannoy et al. 2014)

between γ-CD (66%) and RaMeβ-CD (86%) (Fig. 3.20A). Moreover, the photocatalytic activity increased progressively upon addition of increasing amounts of RaMeβ-CD and a maximum degradation rate of 86% was reached for a RaMeβ-CD/Ti molar ratio of 0.076, which was twice that of the sol-gel TiO_2. Beyond this optimum, a gradual decrease in the photocatalytic activity to 77% and 68% was noticed.

It is worth emphasizing that the combination of good structural and textural properties requires the choice of a correct temperature of calcination. For instance, the TiO_2 material prepared from the RaMeβ-CD/P123 assemblies and calcined at 400 °C presented better textural characteristics (S_{BET} = 158 $m^2\ g^{-1}$; pv = 0.45 $cm^3\ g^{-1}$; ps = 9.3 nm) compared with the material calcined at 500 °C (S_{BET} = 110 $m^2\ g^{-1}$; pv = 0.35 $cm^3\ g^{-1}$; ps = 12.1 nm) (Table 3.3), but it gave lower PAA degradation rates due to the high density of defects at 400 °C (Fig. 3.20B) which should favor the electron-hole recombination. Conversely, above 500 °C, the catalyst was well-crystallized but, the size of the crystallites increased very rapidly (62.5 nm for rutile at 700 °C) resulting in a degradation of the textural characteristics (S_{BET} = 16 $m^2\ g^{-1}$; pv = 0.14 $cm^3\ g^{-1}$ at 700 °C) (Table 3.3). So, the temperature of 500 °C represented the conditions under which an optimal balance of high pore volumes, large surface areas and high crystallinity may be obtained to achieve the optimum photocatalyst for the photodegradation of PAA in water.

The origin of the enhancement of the photocatalytic activity was related to a combined effect of improved textural characteristics and controlled crystalline properties. The high surface areas, which may be correlated with the small size of the crystallites (8–16 nm), should provide a large number of adsorption sites and active centers surrounding the electron-hole pairs, thus facilitating the first step of the photocatalytic reaction. On the other hand, the high pore volumes may allow for more PAA to be adsorbed on the internal surface of the pores, thus improving the diffusion of the substrate to the adsorption sites during the photocatalytic process. Finally, the low density of crystalline defects obtained for the material calcined at 500 °C may produce less grain boundaries and thus, a larger amount of charge carriers should reach the surface of the crystal to initiate the redox reactions.

Taken together, these results showed that the photocatalytic activity of TiO_2 materials may be correlated with their structural and textural characteristics, both of which depend on the concentration and chemical nature of the cyclodextrin employed. Indeed, the strongest effects in the pore volume, surface area, phase composition and photocatalytic activity were observed when RaMeβ-CD was used as structure directing agent and for a calcination temperature of 500 °C. Overall, it was shown that all the above parameters are interlinked and a harmonization between them is necessary to obtain an efficient photocatalyst.

3.4.3.3 Mesoporous Visible-Light Responsive au/TiO_2 Photocatalysts

In recent years, Au/TiO_2 composites have attracted much interest as efficient plasmonic photocatalysts owing to the ability of Au nanoparticles to absorb light in the visible region and TiO_2 to efficiently separate the photogenerated electrons and holes at the metal-semiconductor interface (Kowalska et al. 2009; Wang and Caruso 2011; Wang et al. 2012; Naya et al. 2014). The redox ability of gold nanoparticles actually originates from their localized surface plasmon resonance (LSPR) arising from the collective oscillations of electrons on the nanoparticle surface under light irradiation (Lin et al. 2015) and depends both on particle size and shape (Park et al. 2007). Highly active visible-light Au/TiO_2 photocatalysts were prepared by taking advantage of the ability of cyclodextrins to direct the self-assembly of TiO_2 colloids in a porous network over which Au nanoparticles can be uniformly dispersed (Lannoy et al. 2017). The overall procedure employed for the preparation of Au-modified TiO_2 is schematically illustrated in Fig. 3.21. In a first step, a stable sol made-up of TiO_2 nanoparticles crystallized in anatase (70%) and brookite (30%) is synthesized in water/isopropanol solution (H_2O/Ti = 88) by sol-gel process using titanium isopropoxide ($Ti(OiPr)_4$) as inorganic precursor and nitric acid as peptizing agent (HNO_3/Ti = 0.2) (Bleta et al. 2010). In a second step, the gold salt precursor (chloroauric acid, $HAuCl_4$) was introduced in the titania sol together with various cyclodextrins (α-CD, β-CD, γ-CD, RaMeβ-CD or HPβ-CD). After drying at 60 °C and calcination at 500 °C, a composite material made-up of metallic Au nanoparticles (2.5 wt%,) dispersed on the TiO_2 surface was recovered. In this approach, the cyclodextrin had a dual role, *i.e.* it acted as a structure directing agent to guide the

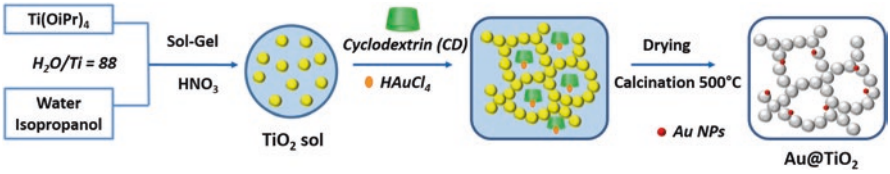

Fig. 3.21 Schematic illustration of the synthesis of mesoporous Au/TiO_2 catalysts where the cyclodextrin acts as structure directing agent to direct the self-assembly of gold and TiO_2 colloids in a nanostructured framework. Reprinted with permission from (Lannoy et al. 2017). Copyright 2017 American Chemical Society

self-assembly of TiO_2 colloids in a nanostructured network and, at the same time, it ensured uniform dispersion of gold nanoparticles over the mesoporous support.

Evidence for the key role of the cyclodextrins in the morphology of Au/TiO_2 composites was provided by electron microscopy. Fig. 3.22 depicts typical field emission scanning electron microscopy (FE-SEM) images of two selected composites prepared with the native β-CD and RaMeβ-CD. Gold nanoparticles were clearly distinguished in all micrographs revealing intimate contact with the mesoporous TiO_2 support. Moreover, it was noticed that, in contrast to β-CD which gave rise to dense and compact structures with sharp angular domains, over which small Au particles were uniformly dispersed (Fig. 3.22a–d), RaMeβ-CD exerted an opposing action, producing a highly porous framework over which Au nanoparticles with larger sizes which sometimes reached or exceeded 200 nm diameter were formed (Fig. 3.22f–i). The average diameter of Au nanoparticles prepared from β-CD was about 15–20 nm Fig. 3.22e), in agreement with XRD data, while two types of particles with average diameters of approximately 15–30 nm and 100–150 nm formed in the presence of RaMeβ-CD (Fig. 3.22j).

The corresponding transmission electron microscopy (TEM) images confirmed the existence of monomodal particles with β-CD (Fig. 3.23a, b) and bimodal particles with RaMeβ-CD (Fig. 3.23c, d). On the other hand, the natives α-CD and γ-CD presented a similar behavior to β-CD, giving rise to small monodisperse particles, while bigger and more polydisperse particles formed with HPβ-CD.

From Fig. 3.24a, b it can be noticed that all CD-derived photocatalysts present enhanced photocatalytic performances compared with the corresponding sol-gel materials. RaMeβ-CD gave rise to the most efficient photocatalysts for the PAA degradation under both UV and visible-light irradiation. The reaction mechanism in these photocatalysts is different depending on whether excitation occurs on the semi-conductor bandgap (bare TiO_2) or on the surface plasmon of gold nanoparticles (Au-modified TiO_2). Thus, in the case of bare TiO_2 which is composed of anatase (Eg = 3.2 eV) and brookite (Eg = 3.3 eV), irradiation with UV-light is necessary to produce positive holes in the valence band (h^+_{VB}) and electrons in the conduction band (e^-_{CB}) (Fig. 3.24c). The photogenerated holes can then oxidize adsorbed water and surface -OH groups (and eventually some PAA molecules), while the photogenerated electrons can reduce molecular oxygen adsorbed on the TiO_2 surface. These reactions can finally lead to the production of hydroxyl radicals

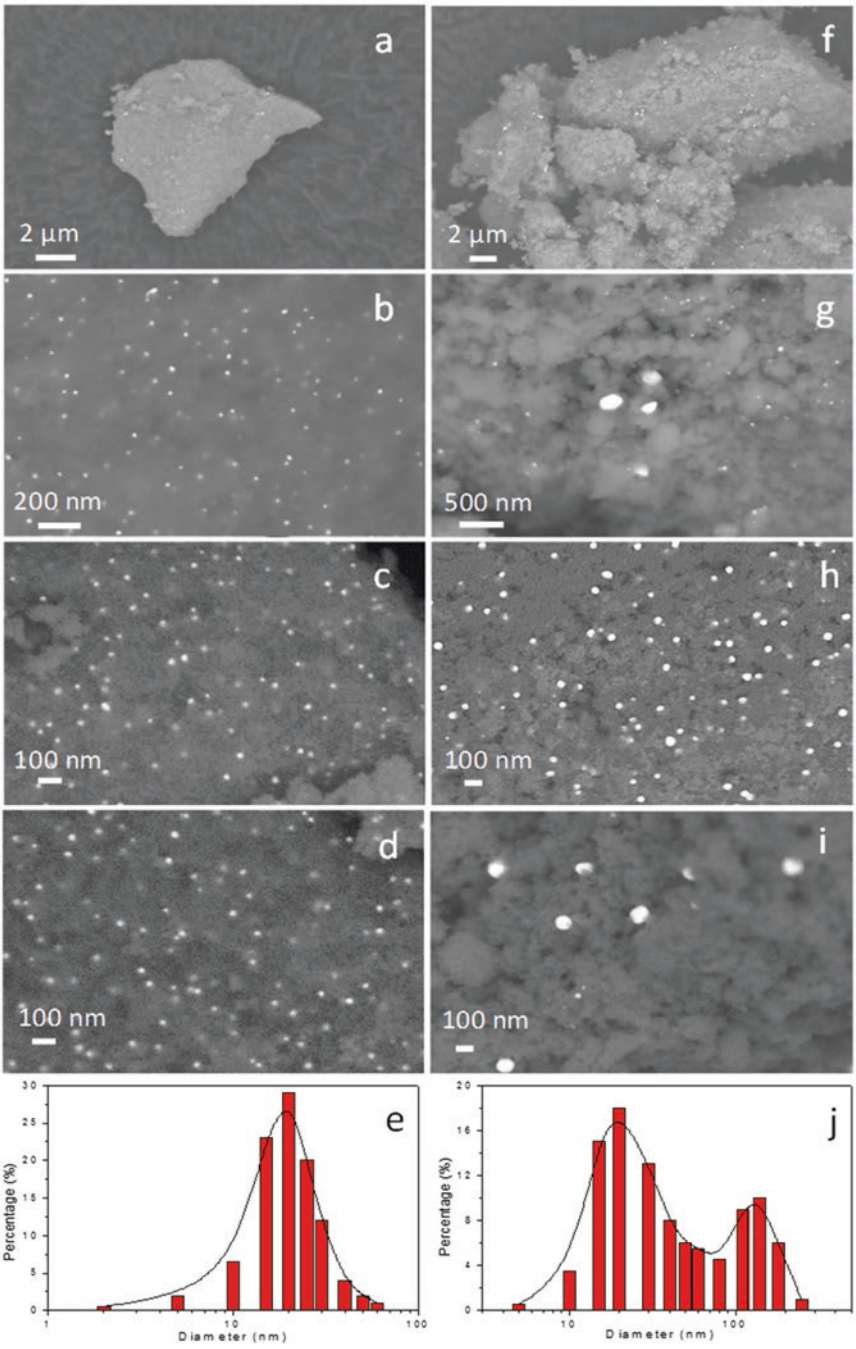

Fig. 3.22 Field emission-scanning electron microscopy (FE-SEM) images recorded with back-scattered electrons on β-CD derived Au/TiO_2 (**a–d**) and RaMeβ-CD derived Au/TiO_2 composites (**f–i**). Corresponding Au particle size distributions for the photocatalysts prepared with β-CD (e) and RaMeβ-CD (j). Reprinted with permission from (Lannoy et al. 2017). Copyright 2017 American Chemical Society

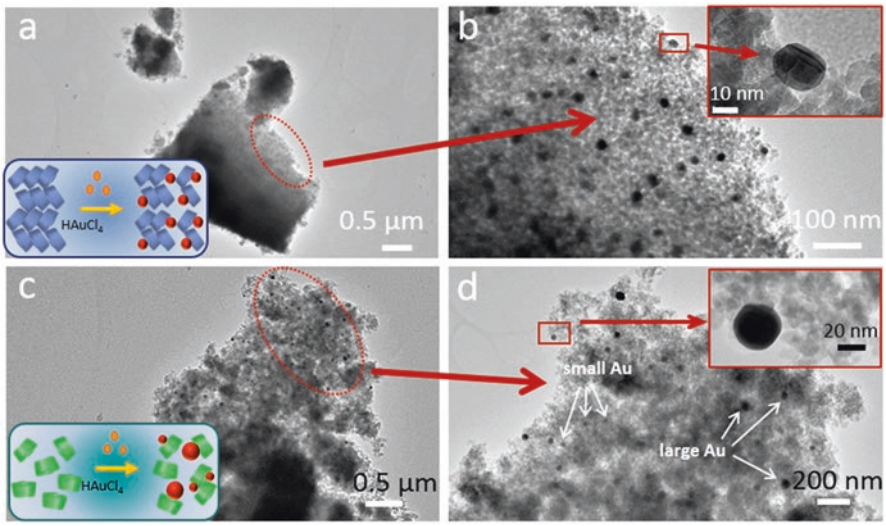

Fig. 3.23 Transmission electron microscopy (TEM) bright-field images of the Au/TiO_2 composites prepared with β-CD (**a, b**) and RaMeβ-CD (**c, d**). Note the formation of monomodal particles with β-CD and bimodal particles with RaMe β-CD. Reprinted with permission from (Lannoy et al. 2017). Copyright 2017 American Chemical Society

($^{\bullet}OH$) and superoxide radical anions ($O_2^{\bullet-}$) respectively, which are powerful oxidants for the degradation of organic pollutants in water. On the other hand, in the case of Au/TiO_2 composites, the electronic charge carriers responsible for the PAA degradation are likely to come mainly from the LSPR excitation of gold nanoparticles under visible light irradiation (Fig. 3.24d). Moreover, as the lifetime of electrons generated in the localized surface plasmon resonance (LSPR) process is very short (less than 10^{-3} ns for Au nanoparticles), their intimate contact with the titania surface should favor the transfer of the hot electrons from the plasmonic Au nanoparticles to the TiO_2 conduction band, thus hindering the e^-/h^+ recombination and enhancing the photocatalytic efficiency (Clavero 2014). On the basis of these results, it was concluded that the effect of cyclodextrins in increasing the porosity of both TiO_2 and Au/TiO_2 photocatalysts follows the order RaMeβ-CD > HPβ-CD > γ-CD ≈ α-CD > β-CD, while their effect in decreasing the size of gold nanoparticles follows an opposite trend, i.e. β-CD > γ-CD > α-CD > RaMeβ-CD > HPβ-CD (Fig. 3.24e, f).

The high photocatalytic activity of Au/TiO_2 prepared from RaMeβ-CD was ascribed to the presence of marked hydrophobic and hydrophilic microenvironments located on both the narrow and wider faces of the ring, conferring to this cyclodextrin an amphiphilic behavior and self-organizing properties at solid-liquid interfaces. Thus, in contrast to native cyclodextrins which are not surface-active and tend to form close-packed crystallites by intermolecular hydrogen bonding (Bleta et al. 2014a; b; c), RaMeβ-CD presents a good combination of surface active properties and weak intermolecular interactions to efficiently direct the self-assembly of titania

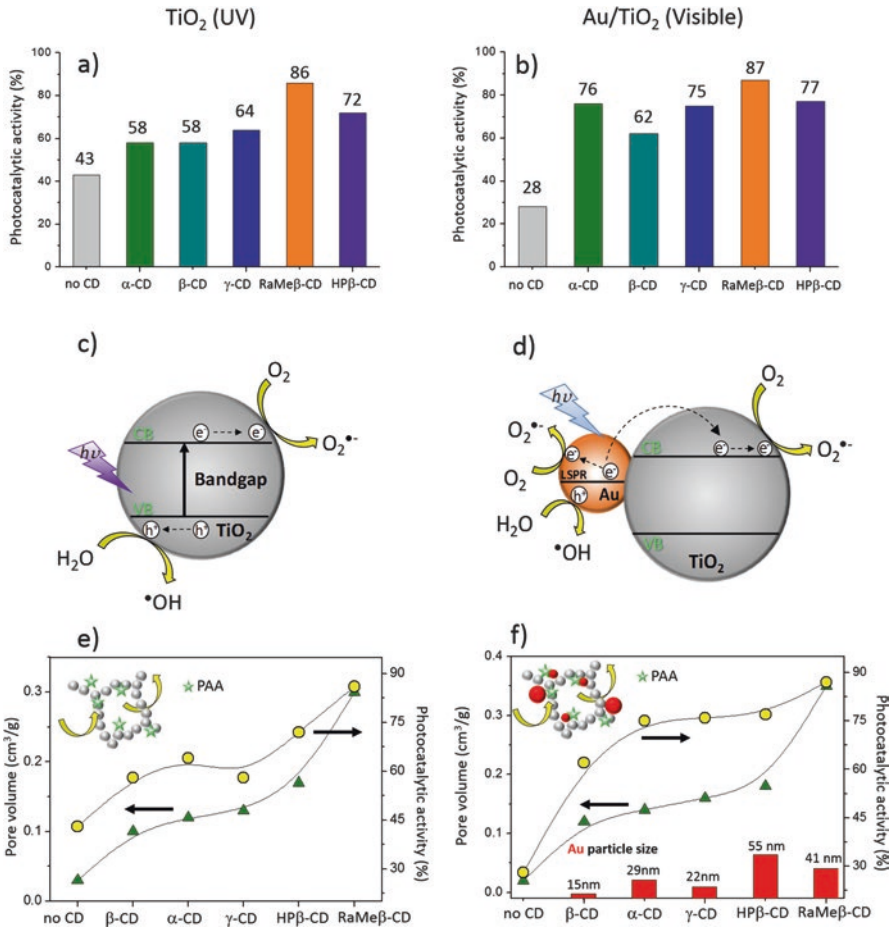

Fig. 3.24 Comparison of the phenoxyacetic acid (PAA) degradation rate after 7 h under UV-light irradiation (360 nm) on bare TiO_2 (**a**), and under visible-light irradiation (420 nm) on Au/TiO_2 (**b**). UV-induced photocatalytic activity by bandgap excitation of TiO_2 (**c**), and visible light-induced photocatalytic activity driven by localized surface plasmon resonance (LSPR) excitation of Au nanoparticles followed by interfacial electron transfer to the conduction band of TiO_2 (**d**). Effect of the pore volume on the photocatalytic activity of bare TiO_2 materials under UV-light irradiation (360 nm) (**e**). Effect of the pore volume and Au particle size on the photocatalytic activity of Au/TiO_2 composites under visible-light irradiation (420 nm) (**f**). Reprinted with permission from (Lannoy et al. 2017). Copyright 2017 American Chemical Society

colloids in a highly porous network over which gold nanoparticles can be uniformly dispersed. Moreover, as a result of the higher lipophilic character of the methoxy groups (-OCH_3) compared to the 2-hydroxypropyl ones (-$OCH_2CH(CH_3)OH$), smoother interfaces are likely to be created with RaMeβ-CD compared to HPβ-CD, thus facilitating the colloidal self-assembly. Consequently, the TiO_2 and Au/TiO_2

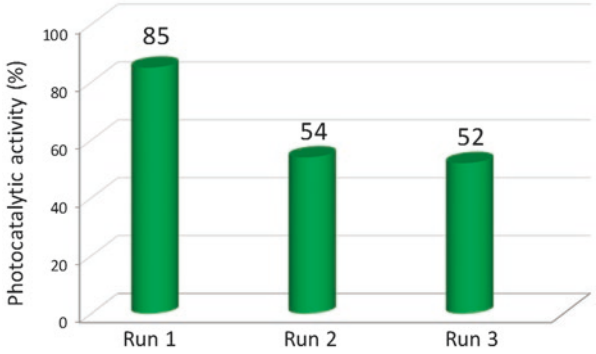

Fig. 3.25 Reusability tests of the RaMeβ-CD derived Au/TiO_2 photocatalyst. The phenoxyacetic acid (PAA) degradation rate was measured after 7 h of exposure under visible-light irradiation (420 nm). Reprinted with permission from (Lannoy et al. 2017, ESI). Copyright 2017 American Chemical Society

photocatalysts prepared from RaMeβ-CD yielded an enhancement of the photocatalytic activity due to a combined effect of good textural characteristics and high crystallinity. Indeed, the large surface area (110 $m^2\ g^{-1}$) should provide a large number of adsorption sites and active centers surrounding the e^-/h^+ pairs, while the high pore volume (0.35 $cm^3\ g^{-1}$) should facilitate the diffusion of PAA molecules towards the adsorption sites during the photocatalytic process. Moreover, the larger Au particles formed within the RaMeβ-CD-derived Au/TiO_2 photocatalysts are likely to improve the photoabsorption in a wider wavelength range, thus increasing the number of absorbed photons (Kowalska et al. 2009). In addition, the existence of gold particles with various dimensions within the same photocatalysts should also facilitate the electron transport from small to large particles through the conduction band of TiO_2 (Naya et al. 2014). Finally, the good crystallinity of both TiO_2 and Au particles may produce less defects and thus enhance the interfacial electron transfer rate between Au nanoparticles and the TiO_2 semi-conductor.

Based on these results, the recyclability and reuse of the most efficient photocatalyst (*i.e.* RaMeβ-CD-derived Au/TiO_2) was evaluated in the degradation of the phenoxyacetic acid (PAA), under visible light irradiation. The photocatalytic activity markedly decreased from 85% to 54% during the second run, then remained almost stable to 52% during the third run. This result was explained by the competitive adsorption and agglomeration of the PAA molecules (as well as the by-products) on the photocatalyst surface through formation of hydrogen bonds between the surface hydroxyls and the carboxylic acid groups of the PAA. Thus, because of the surface coverage with organics after each run, new parts of the photocatalyst surface become unavailable, thus reducing the number of the photocatalytic sites involved in the photoreaction and hindering the adsorption of water molecules, which are key factors in the production of radicals. These results confirmed the fact that the water/semiconductor interface is very important in photocatalysis and the masking of the photocatalytic sites may have a strong impact on the photodegradation efficiency (Fig. 3.25).

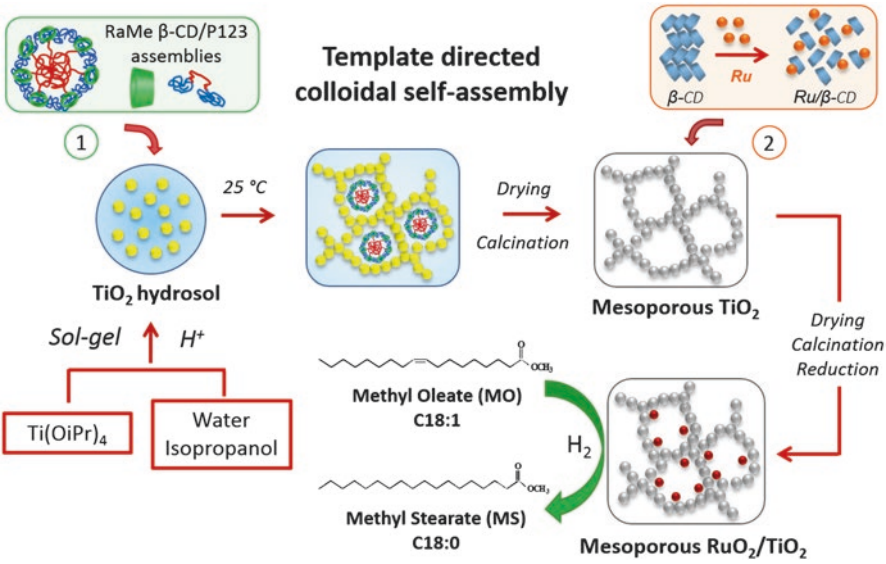

Fig. 3.26 Schematic illustration of the synthesis of RuO_2/TiO_2 composites by RaMeβ-CD-P123-directed colloidal self-assembly. Catalysts were calcined at 400 °C, then reduced under H_2 before being evaluated in the hydrogenation of methyl oleate. Reprinted with permission of the Royal Society of Chemistry from (Bleta et al. 2016)

3.4.3.4 Mesoporous RuO_2/TiO_2 Composites with High Catalytic Performance in the Hydrogenation of Oils

In heterogeneous catalysis, the design of nanostructured support materials with high specific surface area and tailored porosity is of crucial importance for enhancing the catalyst effectiveness (Bell 2003) (Patent No. WO 2015/055672 A1, 2015). Randomly methylated β-CD (RaMeβ-CD) derived mesoporous titania materials were used as efficient matrices for the preparation of RuO_2/TiO_2 composites with high catalytic activity in the hydrogenation of methyl oleate (MO, C18:1) to methyl stearate (MS, C18:0) under mild conditions (Bleta et al. 2016). The mesoporous catalyst were prepared using a two steps synthesis procedure (Fig. 3.26). In a first step the supramolecular assemblies formed between the block copolymer Pluronic P123 and RaMeβ-CD were used as template to prepare a highly porous TiO_2 support. Then, in a second step, Ru nanoparticles were dispersed over the support by impregnation with the assistance of the native β-CD followed by drying and calcination at 400 °C to produce a RuO_2/TiO_2 composite. Before catalytic tests, RuO_2 was reduced in metallic Ru under H_2 flow at 400 °C for 4 h.

To understand the effect of the CD-based assemblies, four RuO_2/TiO_2 composites (2.5 wt% Ru) were prepared using both conventional sol-gel TiO_2 (TiO_2-sg) and nanostructured RaMeβ-CD-P123-templated TiO_2 (TiO_2-ns) as supports, without or with assistance of β-CD as dispersing agent. XRD patterns of the different catalysts (Fig. 3.27A) indicated that similarly to the undoped TiO_2-ns support, Ru2.5TiO_2-ns

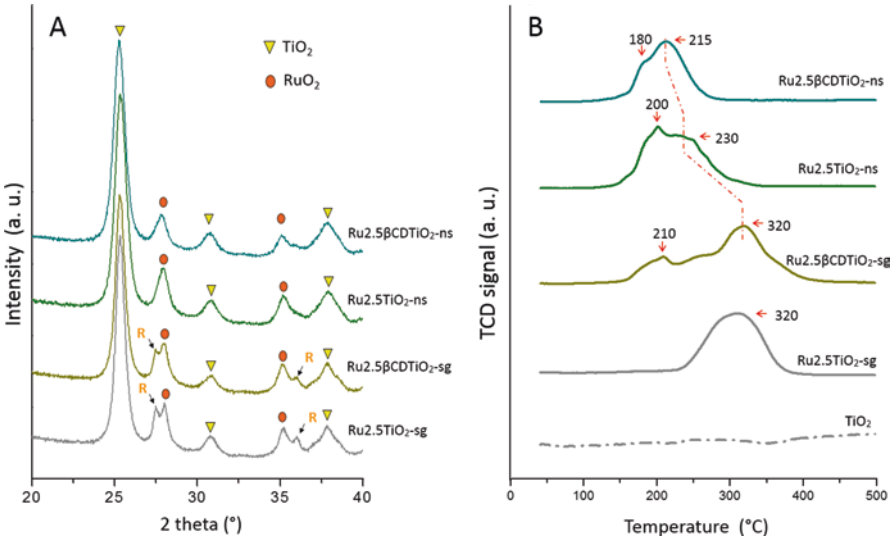

Fig. 3.27 (**A**) X-ray diffraction (XRD) patterns and (**B**) H_2-temperature programed reduction (H_2-TPR) profiles of RuO_2/TiO_2 composites (2.5 wt% Ru) supported over conventional sol-gel TiO_2 (TiO_2-sg) and nanostructured RaMeβ-CD-P123-templated TiO_2 (TiO_2-ns), with or without the assistance of native β-CD as dispersing agent. R denotes the rutile phase. The H_2-TPR profile of the non-doped TiO_2 is added for comparison. Reprinted with permission of the Royal Society of Chemistry from (Bleta et al. 2016)

and Ru2.5β-CDTiO_2-ns catalysts contain only anatase and brookite implying that no anatase-to-rutile or brookite-to-rutile phase transformation occurs during the second calcination at 400 °C. On the other hand, three distinct crystalline phases (anatase, brookite and rutile) were clearly observed for the Ru2.5TiO_2-sg and Ru2.5β-CDTiO_2-sg catalysts. Furthermore, for all materials, additional reflexion lines were clearly observed at $2\theta = 27.8°$ and 34.9° which were indexed to the (110) and (101) planes respectively of the tetragonal RuO_2 (JCPDS 00–043-1027). For the TiO_2-sg supported catalysts, the (110) and (101) planes of RuO_2 and rutile-TiO_2 overlapped due to the lattice matching between these two phases both of which adopt a tetragonal structure. Moreover, it was shown that both the support and the dispersing agent could affect the size of RuO_2 crystallites. Thus, for the Ru2.5 and Ru2.5β-CD catalysts deposited over TiO_2-ns, the crystallite sizes determined from the line broadening of the (110) diffraction peak were 9.8 nm and 9.2 nm respectively, while the average sizes obtained for the catalysts deposited over TiO_2-sg were beyond 10 nm. The H_2-temperature programed reduction (H_2-TPR) profiles indicated that the catalysts supported over nanostructured TiO_2 globally display lower reduction temperatures compared to those supported over conventional sol-gel TiO_2 materials (Fig. 3.27B). This means that the templated-support promotes the formation of small and readily reducible Ru nanoparticles which do not interact strongly with the porous support.

Evidence for the key role of RaMeβ-CD-based assemblies on the dispersion of RuO_2 nanoparticles was provided by high resolution transmission electron microscopy (HR-TEM) combined with high angle annular dark-field scanning transmission electron microscopy (HAADF-STEM). Observations were performed on two selected catalysts, *i.e.* Ru2.5β-CDTiO_2-ns and Ru2.5β-CDTiO_2-sg. From the TEM image shown in Fig. 3.28a, it can be noticed that the surface of the RaMeβ-CD-P123-templated TiO_2 support is decorated with RuO_2 nanoparticles which can be directly visualised by the bright spots resulting from the difference in Z-contrast between the two oxides (Fig. 3.28b). Moreover, energy dispersive spectroscopy (EDS) elemental mapping on different regions of the TEM micrograph (Fig. 3.28c-f) allows to further differentiate the two phases, *i.e.* TiO_2 (white regions) and RuO_2 nanoparticles (dark regions). TiO_2 nanoparticles in this sample contains tetragonal anatase (~15 nm) and orthorhombic brookite (~10 nm) (Fig. 3.28g–h). Interestingly, mesopores of 15–20 nm diameter, resulting from the self-assembly of these nanoparticles around the supramolecular template, can also be clearly visualised in this micrograph (pink circles), in agreement with N_2-adsorption analyses. On the other hand, RuO_2 nanoparticles are more or less spherical and approximately 10–12 nm in size (Fig. 3.28i), in agreement with XRD results. Conversely, the Ru2.5β-CDTiO_2-sg catalyst shows mainly a dense and less porous network (Fig. 3.28j) made-up of anatase (~35%), brookite (~26%) and rutile (~39%) and over which RuO_2 particles tend to form elongated heterogeneous structures (Fig. 3.28k–n). Such unusual epitaxial growth of RuO_2 nanoparticles over rutile-TiO_2 was also observed by Xiang *et al.* (Xiang et al. 2012) and was suggested to result from the structural matching between these two phases which actually share the same type of lattice symmetry (tetragonal) and have very similar lattice parameters (a = 4.59 Å, c = 2.96 Å for rutile-TiO_2 and a = 4.49 Å, c = 3.10 Å for RuO_2).

The performance of the different supported Ru/TiO_2 catalysts was evaluated in the liquid phase hydrogenation of methyl oleate (MO, C18:1) to methyl stearate (MS, C18:0) under mild conditions (40 bar H_2, 50 °C) (Fig. 3.29). Methyl esters of vegetable oils, derived from polyunsaturated fatty acids, can be transformed through partial or complete hydrogenation into saturated fatty acids with improved physical properties (*e.g.* high melting point and oxidative stability) (Philippaerts et al. 2013). Methyl stearate is an important saturated oil obtained from catalytic hydrogenation of unsaturated methyl oleate and widely used as a feedstock for catalytic hydroge-

Fig. 3.28 (continued) catalyst showing uniform dispersion of RuO_2 nanoparticles over the mesoporous RaMeβ-CD-P123-templated TiO_2 material; energy dispersive spectroscopy (EDS) spectra with the electron beam focused first on a white region (TiO_2) (**e**), and then in a dark region (RuO_2) (**f**) of the catalyst images. HR-TEM micrographs of the Ru2.5β-CDTiO_2-ns catalyst indicating uniform dispersion of TiO_2 nanoparticles crystallised in anatase and brookite (**g** and **h**), as well as RuO_2 nanoparticles (5–10 nm) (i) TEM and high resolution (HR) TEM images of the Ru2.5β-CDTiO_2-sg catalyst composed mostly of a nonporous support material showing TiO_2 and RuO_2 nanoparticle aggregation (j-n). Reprinted with permission of the Royal Society of Chemistry from (Bleta et al. 2016)

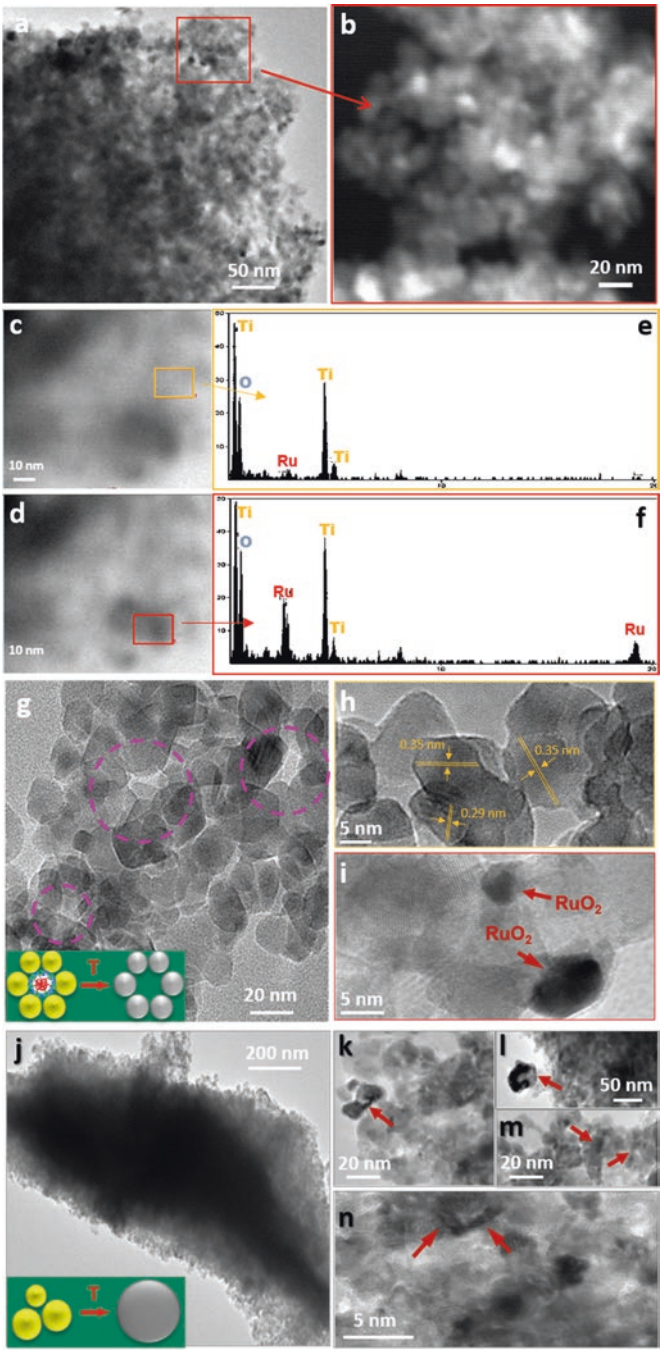

Fig. 3.28 Transmission electron microscopy (TEM) (**a**) and high angle annular dark-field scanning transmission electron microscopy (HAADF-STEM) images (**b–d**) of the Ru2.5β-CDTiO_2-ns

nolysis into its corresponding saturated fatty alcohol (stearyl alcohol, C18:0) (Pritchard et al. 2015). Ru-based catalysts have been shown to be effective for low temperature hydrogenation of carboxylic acid esters, especially for selective hydrogenation of the olefinic C=C bond without affecting the carbonyl C=O bond.

Prior to catalytic tests, RuO_2/TiO_2 composites were pre-treated under hydrogen flow at 400 °C for 4 h to reduce the RuO_2 in metallic Ru. The results obtained after 2 h of reaction (40 bar H_2, 50 °C) with the four catalysts, prepared using either TiO_2-sg or TiO_2-ns support, with the assistance or not of the native β-CD (Ru/β-CD = 11) as dispersing agent, are shown in Fig. 3.29. The results obtained with the non-doped supports (TiO_2-sg and TiO_2-ns) as well as with the Ru2.5 catalyst supported over commercial TiO_2 (Ru2.5TiO_2-A and Ru2.5TiO_2-P25) are added for comparison.

Depending on the preparation method, clear differences can be observed in both the catalytic activity (Fig. 3.29a) and selectivity (Fig. 3.29b). Unlike the control TiO_2-sg and TiO_2-ns supports, which showed almost no activity in the hydrogenation of methyl oleate, all supported Ru/TiO_2 catalysts were selective in the hydrogenation of the olefinic C=C bond producing the fully saturated ester, *i.e.* methyl stearate (C18:0) as the main product and the methyl elaïdate (C18:1, trans-9) as the only byproduct. Moreover, the catalytic performance was strongly affected by the support (TiO_2-sg or TiO_2-ns) and the impregnation method (with or without assistance of native β-CD). Thus, when Ru was deposited over nanostructured RaMeβ-CD-P123-templated TiO_2, the catalytic activity increased sharply from 36% (Ru2.5/TiO_2-sg) to 82% (Ru2.5/TiO_2-ns). Interestingly, the conversion efficiency was further improved when the native β-CD was used as dispersing agent. Thus, the conversion rate increased by ~14% (from 36% to 50%) for the Ru2.5 catalyst deposited over TiO_2-sg and by ~12% (from 82% to 94%) for the same catalyst deposited over TiO_2-ns support. Among the four supported catalysts prepared using the colloidal approach, Ru2.5β-CDTiO_2-ns was the fastest one, achieving almost full MO conversion (~94%) in 2 h. Interestingly, the activity of this catalyst was almost 3-fold higher than that of ruthenium deposited over commercial anatase-TiO_2 (Ru2.5TiO_2-A) and P25-TiO_2 (Ru2.5TiO_2-P25).

Similarly to the catalytic activity, clear differences were observed also in the selectivity toward methyl stearate which increased from 47% to 80% when moving from Ru2.5TiO_2-sg to Ru2.5TiO_2-ns. However, although a beneficial effect of β-CD was noticed for the Ru2.5TiO_2-sg catalyst (MS selectivity increased from 47% to 67%), no clear difference was observed between the Ru2.5TiO_2-ns catalysts prepared without or with assistance of β-CD (MS selectivity was the same ~80%). Over the investigated mesoporous Ru/TiO_2 catalysts, the catalytic performance agreed well with the textural characteristics of the support and the degree of dispersion of the ruthenium species. Indeed, the highest performance of the Ru2.5β-CDTiO_2-ns catalyst resulted from a combined effect of improved textural characteristics of the support and uniform dispersion of ruthenium nanoparticles. Thus, the high surface area of the RaMeβ-CD-P123-templated TiO_2 material (80 $m^2\ g^{-1}$) should provide a high level of dispersion of ruthenium nanoparticles,

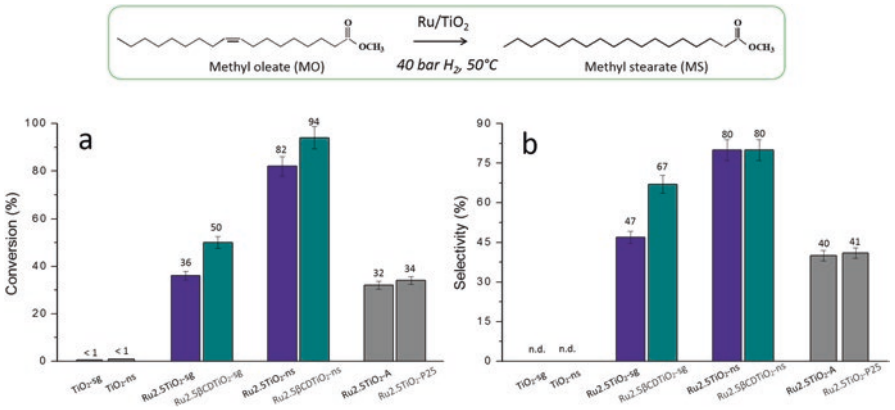

Fig. 3.29 Comparison of the catalytic activity (**a**) and selectivity (**b**) of different supported catalysts in the hydrogenation of methyl oleate (MO, C18:1) to methyl stearate (MS, C18:0). Reaction conditions: Ru (0.02 mmol), methyl oleate (MO/Ru molar ratio = 100), H_2 (40 bar), solvent (heptane, 10 mL), stirring rate (750 rpm), temperature (50 °C), reaction time (2 h). Reprinted with permission of the Royal Society of Chemistry from (Bleta et al. 2016)

facilitating the contact of methyl oleate with the catalyst surface during the hydrogenation reaction. On the other hand, the high pore volume (0.36 $cm^3\ g^{-1}$) should allow for more reactant molecules to be adsorbed to the internal surface of the pores, thus improving the diffusion of reactants and products toward the active phase during the catalytic process. Finally, the use of native β-CD as dispersing agent may allow for reducing the interparticle aggregation thanks to the ability of this cyclodextrin to interact with both $RuNO(NO_3)_3$ and TiO_2 nanoparticles. Overall, these results revealed a dual role played by the CD-based assemblies, *i.e.* an enhancement of the porosity and surface area of the RuO_2/TiO_2 composites and a better dispersion of Ru nanoparticles over the support, parameters that appear to be essential for enhancing the efficacy of the catalyst in the liquid phase hydrogenation of methyl oleate.

Moreover, as leaching and deactivation are common phenomena encountered in any liquid phase hydrogenation reaction, the ease of recovery and reusability of the catalyst are important features that need to be considered. For this purpose, the recyclability of the most efficient catalyst, *i.e.* Ru2.5β-CDTiO_2-ns, was investigated in three successive runs. Remarkably, no loss of activity and selectivity was observed during the consecutive cycles, indicating high stability of the supported catalyst under the employed reaction conditions (Fig. 3.30). The high surface area and large pore volume generated by the template-directed self-assembly of titania colloids should allow for a good dispersion of nanosized ruthenium particles and, therefore, effectively prevent aggregation while improving the chemical stability of the catalyst. Moreover, the thermal treatment at 400 °C should improve fixation of ruthenium species over the TiO_2 material, preventing leaching from the matrix to the reaction media during the catalytic process. The high efficacy of this catalyst

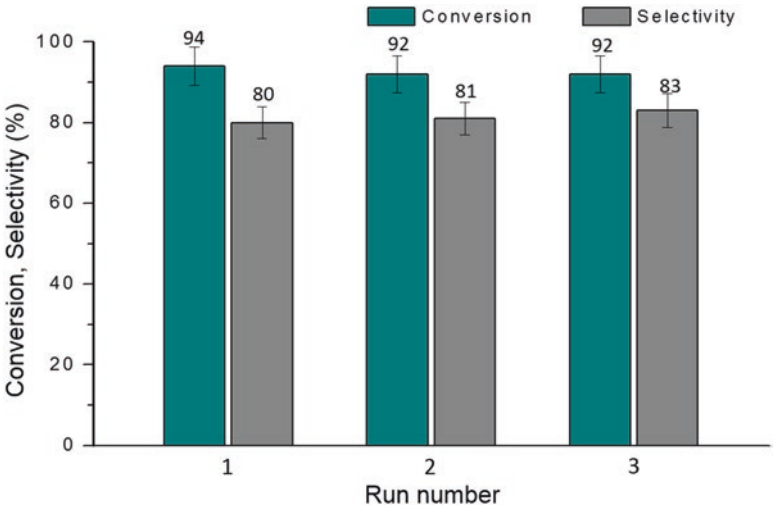

Fig. 3.30 Reusability tests of the Ru2.5β-CDTiO$_2$-ns catalyst. Reaction conditions: methyl oleate/ruthenium molar ratio (MO/Ru = 100), H_2 (40 bar), solvent (heptane, 10 mL), stirring rate (750 rpm), temperature (50 °C), reaction time (2 h). Reprinted with permission of the Royal Society of Chemistry from (Bleta et al. 2016)

combined with ease of recovery and reuse, without loss of conversion and selectivity, makes the colloidal self-assembly a simple and versatile approach for the synthesis of supported catalysts with high performance in liquid phase hydrogenation reactions.

3.5 Conclusion

In this chapter, we presented an overview of the different types of porous inorganic materials that can be prepared from cyclodextrins or cyclodextrin-based assemblies, ranging from microporous to mesoporous materials and further to hierarchically structured porous materials with a three-dimensional interconnected network. From the perspective of the synthesis, the approach that involves hydrolysis and catalytic polycondensation of a silicon alkoxide precursor around a supramolecular template is most commonly used for the fabrication of silica materials. On the other hand, the template-directed colloidal self-assembly approachen ables rational design of a broad range of nanostructured transition metal oxides with very high specific surface areas (380 $m^2\ g^{-1}$ for γ-Al_2O_3 and 110 $m^2\ g^{-1}$ for TiO_2), tailored porosities in the mesoscale (2–20 nm), controlled crystal phase compositions and various morphologies ranging from spheres, to rod-like particles and fibers. Moreover, metal nanoparticles can also be uniformly dispersed within these materials providing nanostructured composites with tunable properties. With respect to catalytic

applications, the cyclodextrin-derived nanostructured porous materials and composites hold great promise owing to their attractive and unique characteristics which are key factors in obtaining highly active, selective, stable and recyclable heterogeneous catalysts.

References

Alphonse P, Bleta R, Lavergne D, Barrault J, Maciuca A, Tatibouët JM, Rossignol C (2015) Patent No. WO 2015/055672 A1

Antonietti M (2006) Silica nanocasting of lyotropic surfactant phases and organized organic matter: material science or an analytical tool? Philos Trans R Soc Lond Ser A 364:2817–2840

Armbrust EV (2009) The life of diatoms in the world's oceans. Nature 459:185–192

Armbrust E, Berges J, Bowler C, Green B, Martinez D, Putnam N, Zhou S, Allen AE, Apt KE, Bechner M, Brzezinski MA, Chaal BK, Chiovitti A, Davis AK, Demarest MS, Detter JC, Glavina T, Goodstein D, Hadi MZ, Hellsten U, Hildebrand M, Jenkins BD, Jurk J, Kapitonov VV, Kröger N, Lau WW, Lane TW, Larimer FW, Lippmeier JC, Lucas S, Medina M, Montsant A, Obornik M, Parker MS, Palenik B, Pazour GJ, Richardson PM, Rynearson TA, Saito MA, Schwartz DC, Thamatrakoln K, Valentin K, Vardi A, Wilkerson FP, Rokhsar D (2004) The genome of the diatom Thalassiosira Pseudonana: ecology, evolution, and metabolism. Science 306:79–86

Beck J, Vartuli J, Roth W, Leonowicz M, Kresge C, Schmitt K, Chu CTW, Olson DH, Sheppard EW, McCullen SB, Higgins JB, Schlenker JL (1992) A new family of mesoporous molecular sieves prepared with liquid crystal templates. J Am Chem Soc 114:10834–10843

Bell A (2003) The impact of nanoscience on heterogeneous catalysis. Science 299:1688–1691

Bernat V, Ringard-Lefebvre C, Bas G, Perly B, Djedaïni-Pilard F, Lesieur S (2008) Inclusion complex of n-octyl β-d-glucopyranoside and α-cyclodextrin in aqueous solutions: thermodynamic and structural characterization. Langmuir 24:3140–3149

Bleta R, Blin J, Stebe M (2006) Solubilization of various fluorocarbons in a fluorinated surfactant/water system: relation with the design of porous materials. J Phys Chem B 110:23547–23556

Bleta R, Alphonse P, Lorenzato L (2010) Nanoparticle route for the preparation in aqueous medium of mesoporous TiO2 with controlled porosity and crystalline framework. J Phys Chem C 114:2039–2048

Bleta R, Jaubert O, Gressier M, Menu M (2011) Rheological behaviour and spectroscopic investigations of cerium-modified AlO(OH) colloidal suspensions. J Colloid Int Sci 363:557–565

Bleta R, Alphonse P, Pin L, Gressier M, Menu M (2012) An efficient route to aqueous phase synthesis of nanocrystalline -Al2O3 with high porosity: from stable boehmite colloids to large pore mesoporous alumina. J Colloid Int Sci 367:120–128

Bleta R, Machut C, Leger B, Monflier E, Ponchel A (2013) Coassembly of block copolymer and randomly methylated β-cyclodextrin: from swollen micelles to mesoporous alumina with tunable pore size. Macromolecules 46:5672–5683

Bleta R, Lannoy A, Machut C, Monflier E, Ponchel A (2014a) Understanding the role of cyclodextrins in the self-assembly, crystallinity, and porosity of titania nanostructures. Langmuir 30:11812–11822

Bleta R, Machut C, Leger B, Monflier E, Ponchel A (2014b) Investigating the effect of randomly methylated β-cyclodextrin/block copolymer molar ratio on the template-directed preparation of mesoporous alumina with tailored porosity. J Incl Phenom Macrocycl Chem 80:323–335

Bleta R, Menuel S, Leger B, Da Costa A, Monflier E, Ponchel A (2014c) Evidence for the existence of crosslinked crystalline domains within cyclodextrin-based supramolecular hydrogels through sol-gel replication. RSC Adv 4:8200–8208

Bleta R, Noel S, Addad A, Ponchel A, Monflier E (2016) Mesoporous RuO_2/TiO_2 composites prepared by cyclodextrin-assisted colloidal self-assembly: towards efficient catalysts for the hydrogenation of methyl oleate. RSC Adv 6:14570–14579

Blin J, Bleta R, Ghanbaja J, Stebe M (2006) Fluorinated emulsions: templates for the direct preparation of macroporous-mesoporous silica with a highly ordered array of large mesopores. Micropor Mesopor Mater 94:74–80

Boal A, Ilhan F, DeRouchey J, Thurn-Albrecht T, Russell T, Rotello V (2000) Self-assembly of nanoparticles into structured spherical and network aggregates. Nature 404:746–748

Born M, Ritter H (1995) Side-chain polyrotaxanes with a tandem structure based on cyclodextrins and a polymethacrylate main chain. Angew Chem Int Ed Engl 34:309–311

Breslow R, Dong S (1998) Biomimetic reactions catalyzed by cyclodextrins and their derivatives. Chem Rev 98:1997–2011

Chen D, Caruso R (2013) Recent progress in the synthesis of spherical titania nanostructures and their applications. Adv Funct Mater 23:1356–1374

Clavero C (2014) Plasmon-induced hot-electron generation at nanoparticle/metal-oxide interfaces for photovoltaic and photocatalytic devices. Nat Photonics 8:95–103

Corma A (1997) From microporous to mesoporous molecular sieve materials and their use in catalysis. Chem Rev 97:2373–2420

Corma A, Moliner M, Diaz-Cabanas MJ, Serna P, Femenia B, Primo J, Garcia H (2008) Biomimetic synthesis of microporous and mesoporous materials at room temperature and neutral pH, with application in electronics, controlled release of chemicals, and catalysis. New J Chem 32:1338–1345

Davis M (2002) Ordered porous materials for emerging applications. Nature 417:813–821

Dreiss C, Nwabunwann E, Liu R, Brooks N (2009) Assembling and de-assembling micelles: competitive interactions of cyclodextrins and drugs with Pluronics. Soft Matter 5:1888–1896

Fujishima A, Honda K (1972) Electrochemical photolysis of water at a semiconductor electrode. Nature 238:37–38

Gaitano G, Brown W, Tardajos G (1997) Inclusion complexes between cyclodextrins and triblock copolymers in aqueous solution: a dynamic and static light-scattering study. J Phys Chem B 101:710–719

Gomathi Devi L, Kavitha R (2013) A review on non-metal ion doped titania for the photocatalytic degradation of organic pollutants under UV/solar light: role of photogenerated charge carrier dynamics in enhancing the activity. Appl Catal B 140-141:559–587

Hamm CE, Merkel R, Springer O, Jurkojc P, Maier C, Prechtel K, Smetacek V (2003) Architecture and material properties of diatom shells provide effective mechanical protection. Nature 421:841–843

Han BH, Antonietti M (2002) Cyclodextrin-based pseudopolyrotaxanes as templates for the generation of porous silica materials. Chem Mater 14:3477–3485

Han BH, Smarsly B, Gruber C, Wenz G (2003) Towards porous silica materials via nanocasting of stable pseudopolyrotaxanes from α-cyclodextrin and polyamines. Microporous Mesoporous Mater 66:127–132

Hao E, Lian T (2000) Layer-by-layer assembly of CdSe nanoparticles based on hydrogen bonding. Langmuir 16:7879–7881

Harada A (1996) Preparation and structures of supramolecules between cyclodextrins and polymers. Coord Chem Rev 148:115–133

Harada A (2001) Cyclodextrin-based molecular machines. Acc Chem Res 34:456–464

Harada A, Kamachi M (1990) Complex formation between poly (ethylene glycol) and α-cyclodextrin. Macromolecules 23:2821–2823

Harada A, Hashidzume A, Yamaguchi H, Takashima Y (2009) Polymeric rotaxanes. Chem Rev 109:5974–6023

Herrmann W, Keller W, Wenz G (1997) Kinetics and thermodynamics of the inclusion of ionene-6, 10 in α-cyclodextrin in an aqueous solution. Macromolecules 30:4966–4972

Hildebrand M (2008) Diatoms, biomineralization processes, and genomics. Chem Rev 108:4855–4874

Holmqvist P, Alexandridis P, Lindman B (1998) Modification of the microstructure in block copolymer-water-"oil" systems by varying the copolymer composition and the "oil" type: small-angle X-ray scattering and deuterium-NMR investigation. J Phys Chem B 102:1149–1158

Imhof A, Pine D (1997) Ordered macroporous materials by emulsion templating. Nature 389:948–951

Jiang B, Guo D, Liu Y (2010) Self-assembly of amphiphilic perylene-cyclodextrin conjugate and vapor sensing for organic amines. J Org Chem 75:7258–7264

Joseph J, Dreiss C, Cosgrove T, Pedersen J (2007) Rupturing polymeric micelles with cyclodextrins. Langmuir 23:460–466

Kooistra W, Gersonde R, Medlin L, Mann D (2007) In: Falkowski PG, Knoll AH (eds) The origin and evolution of diatoms: their adaptation to a planktonic existence. Evolution of primary producers in the sea. Elsevier, Boston, pp 207–249

Kowalska E, Abe R, Ohtani B (2009) Visible light-induced photocatalytic reaction of gold-modified titanium(IV) oxide particles: action spectrum analysis. Chem Commun:241–243

Kresge CT, Leonowicz ME, Roth WJ, Vartuli JC, Beck JS (1992) Ordered mesoporous molecular sieves synthesized by a liquid-crystal template mechanism. Nature 359:710–712

Kröger N, Poulsen N (2008) Diatoms from cell wall biogenesis to nanotechnology. Annu Rev Genet 42:83–107

Kröger N, Deutzmann R, Sumper M (1999) Polycationic peptides from diatom biosilica that direct silica nanosphere formation. Science 286:1129–1132

Lannoy A, Bleta R, Machut C, Monflier E, Ponchel A (2014) Block copolymer-cyclodextrin supramolecular assemblies as soft templates for the synthesis of titania materials with controlled crystallinity, porosity and photocatalytic activity. RSC Adv 4:40061–40070

Lannoy A, Bleta R, Machut-Binkowski C, Addad A, Monflier E, Ponchel A (2017) Cyclodextrin-directed synthesis of gold-modified TiO_2 materials and evaluation of their photocatalytic activity in the removal of a pesticide from water: effect of porosity and particle size. ACS Sustain Chem Eng 5:3623–3630

Lazzara G, Milioto S (2008) Copolymer-cyclodextrin inclusion complexes in water and in the solid state. A physico-chemical study. J Phys Chem B 112:11887–11895

Leclercq L, Bricout H, Tilloy S, Monflier E (2007) Biphasic aqueous organometallic catalysis promoted by cyclodextrins: can surface tension measurements explain the efficiency of chemically modified cyclodextrins? J Colloid Int Sci 307:481–487

Li J, Harada A, Kamashi M (1994) Sol-gel transition during inclusion complex formation between α-cyclodextrin and high molecular weight poly (ethylene glycol)s in aqueous solution. Polym J 26:1019–1026

Lin Z, Wang X, Liu J, Tian Z, Dai L, He B, Han C, Wu Y, Zeng Z, Hu Z (2015) On the role of localized surface plasmon resonance in UV-vis light irradiated au/TiO2 photocatalysis systems: pros and cons. Nanoscale 7:4114–4123

Linsebigler A, Lu G, Yates J (1995) Photocatalysis on TiO_2 surfaces: principles, mechanisms, and selected results. Chem Rev 95:735–758

Liu Y, Goebl J, Yin Y (2013) Templated synthesis of nanostructured materials. Chem Soc Rev 42:2610–2653

Lu AH, Schüth F (2006) Nanocasting: a versatile strategy for creating nanostructured porous materials. Adv Mater 18:1793–1805

Lu C, Wu N, Jiao X, Luo C, Cao W (2003) Micropatterns constructed from au nanoparticles. Chem Commun:1056–1057

Mahata A, Bose D, Ghosh D, Jana B, Bhattacharya B, Sarkar D, Chattopadhyay N (2010) Studies of triton X-165-β-cyclodextrin interactions using both extrinsic and intrinsic fluorescence. J Colloid Int Sci 347:252–259

Naya S, Niwa T, Kume T, Tada H (2014) Visible-light-induced electron transport from small to large nanoparticles in bimodal gold nanoparticle-loaded titanium(IV) oxide. Angew Chem 126:7433–7437

Nogueiras-Nieto L, Alvarez-Lorenzo C, Sandez-Macho I, Concheiro A, Otero-Espinar F (2009) Hydrosoluble cyclodextrin/poloxamer polypseudorotaxanes at the air/water interface, in bulk solution, and in the gel state. J Phys Chem B 113:2773–2782

Nursam N, Wang X, Caruso R (2015) Macro−/mesoporous titania thin films: analysing the effect of pore architecture on photocatalytic activity using high-throughput screening. J Mater Chem A 3:24557–24567

Okumura H, Kawaguchi Y, Harada A (2001) Preparation and characterization of inclusion complexes of poly(dimethylsiloxane)s with cyclodextrins. Macromolecules 34:6338–6343

Ovenstone J (2001) Preparation of novel titania photocatalysts with high activity. J Mater Sci 36:1325–1329

Park J, Momma T, Osaka T (2007) Spectroelectrochemical phenomena on surface plasmon resonance of au nanoparticles immobilized on transparent electrode. Electrochim Acta 52:5914–5923

Patolsky F, Weizmann Y, Lioubashevski O, Willner I (2002) Au-nanoparticle nanowires based on DNA and polylysine templates. Angew Chem Int Ed 41:2323–2327

Periyat P, Pillai S, McCormack D, Colreavy J, Hinder S (2008) Improved high-temperature stability and sun-light-driven photocatalytic activity of sulfur-doped anatase TiO_2. J Phys Chem C 112:7644–7652

Philippaerts A, Jacobs P, Sels B (2013) Is there still a future for hydrogenated vegetable oils ? Angew Chem Int Ed 52:5220–5226

Pillai S, Periyat P, George R, Colreavy J, George R, Hayden H, Seery M, McCormack DE, Corr D, Hinder S (2007) Synthesis of high-temperature stable anatase TiO_2 photocatalyst. J Phys Chem C 111:1605–1611

Polarz S, Antonietti M (2002) Porous materials via nanocasting procedures: innovative materials and learning about soft-matter organization. Chem Commun:2593–2604

Polarz S, Smarsly B, Bronstein L, Antonietti M (2001) From cyclodextrin assemblies to porous materials by silica templating. Angew Chem Int Ed 40:4417–4421

Poulsen N, Kröger N (2004) Silica morphogenesis by alternative processing of silaffins in the diatom Thalassiosira Pseudonana. J Biol Chem 279:42993–42999

Pritchard J, Filonenko G, van Putten R, Hensen E, Pidko E (2015) Heterogeneous and homogeneous catalysis for the hydrogenation of carboxylic acid derivatives: history, advances and future directions. Chem Soc Rev 44:3808–3833

Rajh T, Micic O, Nozik A (1993) Synthesis and characterization of surface-modified colloidal CdTe qunatum dots. J Phys Chem 97:11999–12003

Saenger W (1980) Cyclodextrin inclusion compounds in research and industry. Angew Chem Int Ed Engl 19:344–362

Singh H, Saquib M, Haque M, Muneer M, Bahnemann D (2007) Titanium dioxide mediated photocatalysed degradation of phenoxyacetic acid and 2,4,5-trichlorophenoxyacetic acid in aqueous suspensions. J Mol Catal A Chem 264:66–72

Su B, Sanchez C, Yang X (2012) Hierarchically structured porous materials, From Nanoscience to catalysis, separation, optics, energy, and life science. Wiley-VCH, Weinheim

Sumper M, Hett R, Lehmann G, Wenzl S (2007) A code for lysine modifications of a silica biomineralizing silaffin protein. Angew Chem Int Ed 46:8405–8408

Sun M, Huang S, Chen L, Li Y, Yang X, Yuan Z, Su B (2016) Applications of hierarchically structured porous materials from energy storage and conversion, catalysis, photocatalysis, adsorption, separation, and sensing to biomedicine. Chem Soc Rev 45:3479–3563

Szejtli J (1998) Introduction and general overview of cyclodextrin chemistry. Chem Rev 98:1743–1753

Travelet C, Schlatter G, Hebraud P, Brochon C, Lapp A, Anokhin D, Ivanov DA, Gaillard C, Hadziioannou G (2008) Multiblock copolymer behaviour of α-CD/PEO-based polyrotaxanes: towards nano-cylinder self-organization of α-CDs. Soft Matter 4:1855–1860

Travelet C, Schlatter G, Hebraud P, Brochon C, Lapp A, Hadziioannou G (2009) Formation and self-organization kinetics of α-CD/PEO-based pseudo-polyrotaxanes in water. A specific behavior at 30 °C. Langmuir 25:8723–8734

Travelet C, Hebraud P, Perry C, Brochon C, Hadziioannou G, Lapp A, Schlatter G (2010) Temperature-dependent structure of α-CD/PEO-based polyrotaxanes in concentrated solution in DMSO: kinetics and multiblock copolymer behavior. Macromolecules 43:1915–1921

Tsai C, Zhang W, Wang C, Van Horn R, Graham M, Huang J, Chen Y, Guo M, Cheng S (2010) Evidence of formation of site-selective inclusion complexation between β-cyclodextrin and poly(ethylene oxide)-block-poly(propylene oxide)-block poly(ethylene oxide) copolymers. J Chem Phys 132:1–9

Uekama K, Irie T (1987) Cyclodextrins and their industrial uses. In: Duchêne D (ed) Pharmaceutical applications of methylated cyclodextrin derivatives. Editions de la Santé, Paris, pp 395–439

Valero M, Grillo I, Dreiss C (2012) Rupture of Pluronic micelles by di-methylated β-cyclodextrin is not due to polypseudorotaxane formation. J Phys Chem B 116:1273–1281

Van Der Voort P, Vercaemst C, Schaubroeck D, Verpoort F (2008) Ordered mesoporous materials at the beginning of the third millennium: new strategies to create hybrid and non-siliceous variants. Phys Chem Chem Phys 10:347–360

Velev O, Kaler E (2000) Structured porous materials via colloidal crystal templating: from inorganic oxides to metals. Adv Mater 7:531–534

Walcarius A (2013) Mesoporous materials and electrochemistry. Chem Soc Rev 42:4098–4140

Wan Y, Zhao D (2007) On the controllable soft-templating approach to mesoporous silicates. Chem Rev 107:2821–2859

Wang X, Caruso R (2011) Enhancing photocatalytic activity of titania materials by using porous structures and the addition of gold nanoparticles. J Mater Chem 21:20–28

Wang X, Blackford M, Prince K, Caruso RA (2012) Preparation of boron-doped porous titania networks containing gold nanoparticles with enhanced visible-light photocatalytic activity. ACS Appl Mater Interfaces 4:476–482

Wang X, Cao L, Chen D, Caruso R (2013) Engineering of monodisperse mesoporous titania beads for photocatalytic applications. ACS Appl Mater Interfaces 5:9421–9428

Weickenmeier M, Wenz G (1997) Threading of cyclodextrins onto a polyester of octanedicarboxylic acid and polyethylene glycol. Macromol Rapid Commun 18:1109–1115

Wenz G (1994) Cyclodextrins as building blocks for supramolecular structures and functional units. Angew Chem Int Ed Engl 33:803–822

Xiang G, Shi X, Wu Y, Zhuang J, Wang X (2012) Size effects in atomic-level epitaxial redistribution process of RuO_2 over TiO_2. Sci Rep 2(801):1–6

Yang H, Sun C, Qiao S, Zou J, Liu G, Smith S, Cheng HM, Lu G (2008) Anatase TiO2 single crystals with a large percentage of reactive facets. Nature 453:638–641

Yang X, Chen L, Li Y, Rooke J, Sanchez C, Su B (2017) Hierarchically porous materials: synthesis strategies and structure design. Chem Soc Rev 46:481–558

Yu W, Peng X (2002) Formation of high-quality CdS and other II−VI semiconductor nanocrystals in noncoordinating solvents: tunable reactivity of monomers. Angew Chem Int Ed 41:2368–2371

Zhang H, Banfield J (1998) Thermodynamic analysis of phase stability of nanocrystalline titania. J Mater Chem 8:2073–2076

Zhang H, Banfield J (2000) Understanding polymorphic phase transformation behavior during growth of nanocrystalline aggregates: insights from TiO2. J Phys Chem B 104:3481–3487

Zhang X, Yang Z, Li X, Deng N, Qian S (2013) β-cyclodextrin's orientation onto TiO_2 and its paradoxical role in guest's photodegradation. Chem Commun 49:825–827

Zhao W, Ma W, Chen C, Zhao J, Shuai Z (2004) Efficient degradation of toxic organic pollutants with Ni2O3/TiO2-x Bx under visible irradiation. J Am Chem Soc 126:4782–4783

Zhu C, Du D, Eychmüller A, Lin Y (2015) Engineering ordered and nonordered porous noble metal nanostructures: synthesis, assembly, and their applications in electrochemistry. Chem Rev 115:8896–8943